



**The Atlas3D project -- III. A census of the stellar angular momentum within the effective radius of early-type galaxies: unveiling the distribution of Fast and Slow Rotators**

|                               |  |
|-------------------------------|--|
| Journal:                      | <i>Monthly Notices of the Royal Astronomical Society</i>   |
| Manuscript ID:                | MN-10-2332-MJ.R1   |
| Wiley - Manuscript type:      | Main Journal   |
| Date Submitted by the Author: | 27-Jan-2011  |
| Complete List of Authors:     | Emsellem, Eric; ESO  |
| Keywords:                     | (classification, colours, luminosities, masses, radii, etc.) < Galaxies, galaxies: elliptical and lenticular, cD < Galaxies, galaxies: kinematics and dynamics < Galaxies, galaxies: structure < Galaxies, galaxies: fundamental parameters < Galaxies |
|                               |  |

# The ATLAS<sup>3D</sup> project – III. A census of the stellar angular momentum within the effective radius of early-type galaxies: unveiling the distribution of Fast and Slow Rotators

Eric Emsellem,<sup>1,2\*</sup> Michele Cappellari,<sup>3</sup> Davor Krajnović,<sup>1</sup> Katherine Alatalo,<sup>4</sup> Leo Blitz,<sup>4</sup> Maxime Bois,<sup>1,2</sup> Frédéric Bournaud,<sup>5</sup> Martin Bureau,<sup>3</sup> Roger L. Davies,<sup>3</sup> Timothy A. Davis,<sup>3</sup> P. T. de Zeeuw,<sup>1,6</sup> Sadegh Khochfar,<sup>7</sup> Harald Kuntschner,<sup>8</sup> Pierre-Yves Lablanche,<sup>2</sup> Richard M. McDermid,<sup>9</sup> Raffaella Morganti,<sup>10,11</sup> Thorsten Naab,<sup>12</sup> Tom Oosterloo,<sup>10,11</sup> Marc Sarzi,<sup>13</sup> Nicholas Scott,<sup>3</sup> Paolo Serra,<sup>10</sup> Glenn van de Ven,<sup>14</sup> Anne-Marie Weijmans,<sup>15</sup>† and Lisa M. Young,<sup>16</sup>

<sup>1</sup>European Southern Observatory, Karl-Schwarzschild-Str. 2, 85748 Garching, Germany

<sup>2</sup>Université Lyon 1, Observatoire de Lyon, Centre de Recherche Astrophysique de Lyon  
and Ecole Normale Supérieure de Lyon, 9 avenue Charles André, F-69230 Saint-Genis Laval, France

<sup>3</sup>Sub-department of Astrophysics, University of Oxford, Denys Wilkinson Building, Keble Road, Oxford OX1 3RH, UK

<sup>4</sup>Department of Astronomy, Campbell Hall, University of California, Berkeley, CA 94720, USA

<sup>5</sup>Laboratoire AIM Paris-Saclay, CEA/IRFU/Sap – CNRS – Université Paris Diderot, 91191 Gif-sur-Yvette Cedex, France

<sup>6</sup>Sterrewacht Leiden, Leiden University, Postbus 9513, 2300 RA Leiden, the Netherlands

<sup>7</sup>Max-Planck Institut für extraterrestrische Physik, PO Box 1312, D-85478 Garching, Germany

<sup>8</sup>Space Telescope European Coordinating Facility, European Southern Observatory, Karl-Schwarzschild-Str. 2, 85748 Garching, Germany

<sup>9</sup>Gemini Observatory, Northern Operations Centre, 670 N. A‘ohoku Place, Hilo, HI 96720, USA

<sup>10</sup>Netherlands Institute for Radio Astronomy (ASTRON), Postbus 2, 7990 AA Dwingeloo, The Netherlands

<sup>11</sup>Kapteyn Astronomical Institute, University of Groningen, Postbus 800, 9700 AV Groningen, The Netherlands

<sup>12</sup>Max-Planck-Institut für Astrophysik, Karl-Schwarzschild-Str. 1, 85741 Garching, Germany

<sup>13</sup>Centre for Astrophysics Research, University of Hertfordshire, Hatfield, Herts AL1 9AB, UK

<sup>14</sup>Max-Planck-Institut für Astronomie, Königstuhl 17, 69117 Heidelberg, Germany

<sup>15</sup>Dunlap Institute for Astronomy & Astrophysics, University of Toronto, 50 St. George Street, Toronto, ON M5S 3H4, Canada

<sup>16</sup>Physics Department, New Mexico Institute of Mining and Technology, Socorro, NM 87801, USA

27 January 2011

**ABSTRACT**

We provide a census of the apparent stellar angular momentum within one effective radius of a volume-limited sample of 260 early-type galaxies (ETGs) in the nearby Universe, using integral-field spectroscopy obtained in the course of the ATLAS<sup>3D</sup> project. We exploit the  $\lambda_R$  parameter (previously used via a constant threshold value of 0.1) to characterise the existence of two families of ETGs: Slow Rotators which exhibit complex stellar velocity fields and often include stellar kinematically distinct cores, and Fast Rotators which have regular velocity fields. Our complete sample of 260 ETGs leads to a new criterion to disentangle Fast and Slow Rotators which now includes a dependency on the apparent ellipticity  $\epsilon$ . It separates the two classes significantly better than the previous prescription, and than a criterion based on  $V/\sigma$ : Slow Rotators and Fast Rotators have  $\lambda_R$  lower and larger than  $k_{FS} \times \sqrt{\epsilon}$ , respectively, where  $k_{FS} = 0.31$  for measurements made within an effective radius  $R_e$ .

We show that the vast majority of early-type galaxies are Fast Rotators: these have regular stellar rotation, with aligned photometric and kinematic axes (Krajnović et al. 2011, Paper II), include discs and often bars and represent  $86 \pm 2\%$  (224/260) of all early-type galaxies in the volume-limited ATLAS<sup>3D</sup> sample. Fast Rotators span the full range of apparent ellipticities from  $\epsilon = 0$  to 0.85, and we suggest that they cover intrinsic ellipticities from about 0.35 to 0.85, the most flattened having morphologies consistent with spiral galaxies. Only a small fraction of ETGs are Slow Rotators representing  $14 \pm 2\%$  (36/260) of the ATLAS<sup>3D</sup> sample of ETGs. Of all Slow Rotators, 11% (4/36) exhibit two counter-rotating stellar disc-like components and are rather low mass objects ( $M_{\text{dyn}} < 10^{10.5} M_{\odot}$ ). All other Slow Rotators (32/36) appear relatively round on the sky ( $\epsilon_e < 0.4$ ), tend to be massive ( $M_{\text{dyn}} > 10^{10.5} M_{\odot}$ ), and often (17/32) exhibit Kinematically Distinct Cores. Slow Rotators dominate the high mass end of ETGs in the ATLAS<sup>3D</sup> sample, with only about one fourth of galaxies with masses above  $10^{11.5} M_{\odot}$  being Fast Rotators. **We show that the  $a_4$  parameter which quantifies the isophotes disciness or boxiness does not seem to be simply related with the observed kinematics, while our new criterion based on  $\lambda_R$  and  $\epsilon$  is nearly independent from the viewing angles.** We further demonstrate that the separation of ETGs in E's (ellipticals) and S0's (lenticulars) is misleading. Slow and Fast Rotators tend to be classified as ellipticals and lenticulars, respectively, but the contamination is strong enough to affect results **solely** based on such a scheme: 20% of all Fast Rotators are classified as E's, and more importantly 66% of all E's in the ATLAS<sup>3D</sup> sample are Fast Rotators.

Fast and Slow Rotators illustrate the variety of complex processes shaping galactic systems, such as e.g., secular evolution, disc instabilities, interaction and merging, gas accretion, stripping and harassment, forming a sequence from high to low (stellar) baryonic angular momentum. Massive Slow Rotators represent the extreme instances within the red sequence of galaxies which might have suffered from significant merging without being able to rebuild a fast rotating component within one effective radius. We therefore argue for a shift in the paradigm for early-type galaxies, where the vast majority of ETGs are galaxies consistent with nearly oblate systems (with or without bars), and where only a small fraction of them (less than 12%) have central (mildly) triaxial structures.

**Key words:** galaxies: elliptical and lenticular, cD – galaxies: evolution – galaxies: formation – galaxies: kinematics and dynamics – galaxies: structure

**1 INTRODUCTION**

Early-type galaxies lie at one end of the Hubble tuning fork, the schematic ordering of galaxy morphology classes established long ago (Hubble 1936; de Vaucouleurs et al. 1991), the late-type spirals being located at the other end of the diagram (excluding irregulars). Although the Hubble sequence is not thought to represent an evolutionary sequence, early-type systems are generally considered to be the output of violent and extreme processes mainly driven by interactions and mergers in a hierarchical Universe, contrasting with formation processes advocated for spiral galaxies.

At moderate to high redshifts, the difficulty to obtain detailed photometric and spectroscopic information of large numbers of systems often lead to gather early-type galaxies into a single class: early-type galaxies are generally viewed as a single family of objects, separated from the line of spiral systems, and which can be studied at various redshifts (e.g. Bell et al. 2004; McIntosh et al. 2005; Kriek et al. 2008). There are nowadays various techniques to build samples of early-type galaxies from large surveys, e.g., colour/spectroscopic information based on the fact that most galaxies in the red sequence are early-type (see e.g. Bell et al. 2004, and references therein). This obviously includes visual classification which, when applied at relatively lower redshift, can lead to a classification closer to the full-fledged schemes defined by Hubble or de Vaucouleurs (Fukugita et al. 2007).

\* E-mail: eric.emsellem@eso.org

† Dunlap Fellow

For nearby samples of galaxies, early-type galaxies are more commonly separated into two groups, namely the ellipticals (E's) and lenticulars (S0's), the latter being a transition class to (or from) the spiral systems (Hubble 1936). This is the existing *paradigm for early-type galaxies*, nicely illustrated by e.g., the work conducted by Bernardi et al. (2010) who studied a large set of galaxies extracted from the Sloan Digital Sky Survey. Early-type galaxies are mostly red-sequence objects, comprising E's (ellipticals) and S0's (lenticulars), each class representing about *half of such a magnitude limited sample of early-type galaxies*. All together, Es and S0s represent a significant fraction ( $\sim 40\%$ ) of the total stellar mass density in the nearby Universe (Bernardi et al. 2010; Fukugita et al. 2007). Ellipticals are thought to be nearly pure spheroidal objects, sometimes with central discs, while lenticulars are disc galaxies with large bulges/spheroidal components. Ellipticals are on average rounder than lenticulars, with very few E's having ellipticities higher than 0.4, and dominate the high-mass range of early-type galaxies.

This picture has been regularly and significantly updated specifically for galaxies in the nearby Universe for which we often have exquisite photometric and spectroscopic information (Bender et al. 1994; Rix et al. 1999; Gerhard et al. 1999). An attempt to, for instance, further refine the elliptical E class into the boxy and discy systems was pursued by Kormendy & Bender (1996): the proposed classification recognises the sequence of intrinsic flattening and shapes and tries to address the presence of discs (Rix & White 1990; Scorza & van den Bosch 1998; Naab & Burkert 2001) and the dynamical status of these galaxies via a photometric proxy (namely,  $a_4$  representing part of the deviation of isophotes from pure ellipses). This has been recently expanded in the context of "light deficit/excess" (Graham & Guzmán 2003; Graham 2004; Ferrarese et al. 2006; Côté et al. 2006; Kormendy et al. 2009) to examine whether or not different groups of ellipticals may be key to link photometric properties with their formation and assembly scenarios (Naab et al. 1999; Khochfar & Burkert 2005; Kormendy et al. 2009; Hopkins et al. 2009a,c). Nevertheless, early-type galaxies continue to be divided into ellipticals (spheroidal-like) and lenticular (disc-like) systems, the former exhibiting some mild triaxiality (usually associated with anisotropy), while the latter are prone to typical disc perturbations, such as e.g., bars.

There are many complications associated to these classification schemes due to e.g., inclination effects or the limitations of photometric measurements (Kormendy & Bender 1996; Cappellari et al. 2007). It is hard to disentangle lenticulars from ellipticals, which limits the conclusions from studies using these as prime ingredients. Emsellem et al. (2007, hereafter E+07) have emphasised the fact that stellar kinematics contain critical information on the actual dynamical status of the galaxy. E+07 suggested that  $\lambda_R$ , a simple parameter which can be derived from the first two stellar velocity moments, can be used as a robust estimator of the apparent specific angular moment (in stars) of galaxies (see also Jesseit et al. 2009).

Following this prescription, E+07 and Cappellari et al. (2007, hereafter C+07) have shown that early-type galaxies are distributed within two broad families depending on their  $\lambda_R$  values: Slow Rotators ( $\lambda_R < 0.1$ ), which show little or no rotation, significant misalignments between the photometric and the kinematic axes, and contain kinematically decoupled components; and Fast Rotators ( $\lambda_R \geq 0.1$ ) which exhibit regular stellar velocity fields, consistent with disc-like rotation (Krajnović et al. 2008) and sometimes bars. These results were, however, based on a representative (but

not complete) sample of 48 early-type galaxies that is not a fair sample of the local Universe.

We are now in a position to re-examine these issues in the light of the volume-limited ATLAS<sup>3D</sup> survey (Cappellari et al. 2011a, hereafter, Paper I). In the present paper, we wish to establish a census of the stellar angular momentum of early-type galaxies (ETGs hereafter) in their central regions via  $\lambda_R$ , and examine how we can relate such a measurement to their formation processes. We will show that a kinematic classification based on  $\lambda_R$  is a more natural and physically motivated way of classifying galaxies. More importantly, we find that galaxies classified as Fast Rotators, based on a refined criterion for  $\lambda_R$ , represent 86% of this magnitude limited sample of ETGs, spread over a large range of flattening, the higher end being within the range covered by spirals. Slow Rotators comprise 14% of the ATLAS<sup>3D</sup> sample, with about 12% of massive early-type galaxies with very low rotation and often with Kinematically Decoupled Components, plus about 2% of lower-mass flattened systems which represent the special case of counter-rotating disc-like components.

In Section 2 we briefly describe the observations we are using for this study. Section 3 is dedicated to a first presentation of the measurements, mainly  $\lambda_R$  and its relation to other basic properties such as ellipticity and dynamical mass. In Section 4 we use these measurements to update our view on Fast and Slow Rotators and propose a new criterion based on simple dynamical arguments. We discuss the corresponding results in Section 5 and conclude in Section 6.

## 2 OBSERVATIONAL MATERIAL AND ANALYSIS

The ATLAS<sup>3D</sup> project is based on a volume-limited sample of 260 targets extracted from a complete sample of early-type galaxies (ETGs). A detailed description of the selection process and properties for the sample are given in (Cappellari et al. 2011a, hereafter Paper I), so we only provide a summary here. The parent sample is comprised of all galaxies within a volume of 42 Mpc, brighter than  $M_K = -21.5$  mag (2MASS, see Jarrett et al. 2000) and constrained by observability ( $|\delta - 29^\circ| < 35$  and away from the Galactic equatorial plane). All 871 galaxies were examined via DSS and SDSS colour images to classify them as ETGs (e.g., absence of clear spiral arms; see Paper I).

The present study mostly relies on integral-field spectroscopic data from the SAURON instrument (Bacon et al. 2001) mounted on the William Herschel Telescope (La Palma, Canary Islands). We have also made use of imaging data obtained from several facilities, including SDSS DR7 (Abazajian et al. 2009), INT and MDM (see Paper I for details). In the next Section, we briefly describe the corresponding imaging and SAURON datasets and its analysis.

### 2.1 Photometric parameters

Various parameters were extracted from the imaging data at our disposal. We first derived radial profiles for all standard variables such as ellipticity  $\epsilon$ , position angle  $PA_{phot}$ , semi-major axis  $a$  and disciness/boxiness as given by  $a_4$  from a best fit ellipse routine, making use of the adapted functionality in the kinemetry routines of Krajnović et al. (2006). The moment ellipticity  $\epsilon$  profiles were computed within radially growing isophotes via the diagonalisation of the inertia tensor as in e.g. C+07. This departs from a simple luminosity-weighted average of the ellipticity profile, which is more strongly biased towards the central values. For these profiles,

#### 4 *Eric Emsellem et al.*

we associate the "aperture" radii  $R$ : for a given elliptical aperture or isophote with an area  $\mathcal{A}$ ,  $R$  is defined as the radius of the circle having the same area  $\mathcal{A} = \pi R^2$ . These profiles (curves of growth) are then interpolated to obtain parameter values at e.g., one (or half) an effective radius  $R_e$  (provided in Table 5 of Paper I). To build diagrams together with quantities derived via the SAURON integral-field data (see next Section), we use ellipse and position angle profiles provided by the photometry and limit the aperture radius  $R$  to a maximum value  $R_S$ : **it is the minimum between the considered radius (e.g.,  $1 R_e$ ) and the radius  $R_{max}$  for which the corresponding ellipse differs in area not more than 15% from the actual field coverage provided by our spectrographic data, with the ellipse itself lying at least 75% within that field of view. This guarantees that we have both a good coverage in area (85%) and that the SAURON spaxels reach sufficiently far out with respect to the borders of the considered aperture. Changing these criteria only affects the measured aperture values for a few systems, and does not modify the global results presented here. These radial profiles were extracted from the available ground-based data. For most of the galaxies, we relied on the green g band, close to the wavelength range covered with the SAURON datacubes. For only a few galaxies, when the g band data was not available or of poor quality, we instead relied on the red r band or even on the SAURON images reconstructed directly from the datacubes: the data used for each individual galaxy is indicated in Table B1.**

A number of galaxies in our sample exhibit strong bars (e.g. NGC 936, NGC 6548, see Krajnović et al. 2011, hereafter Paper II). When the galaxy is viewed at rather low inclination (close to face-on), the bar strongly influences the measured position angle (as well as the ellipticity), implying a strong misalignment between the photometric and kinematic major-axes. The (stellar) kinematic major-axis is an excellent indicator of the line of nodes of a disc galaxy, even when the galaxy hosts a relatively strong bar, and this kinematic axis generally coincides with the outer photometric major-axis outside the bar, where the light distribution is dominated by a disc. The measured flattening does however not properly reflect the intrinsic flattening of the galaxy when measured in the region of the bar. In galaxies with obvious bars, such as NGC 936, NGC 3400, NGC 3412, NGC 3599, NGC 3757, NGC 3941, NGC 4262, NGC 4267, NGC 4477, NGC 4608, NGC 4624, NGC 4733, NGC 4754, NGC 5473, NGC 5770, NGC 6548, UGC 6062, we therefore use the global kinematic position angle, as derived from the two-dimensional SAURON stellar kinematics, with the moment ellipticity value from the outer parts of the galaxy (outside the region influenced by the bar; values provided in Paper II), both for the derivation of e.g.,  $\lambda_R$ , and for all plots of the present paper.

## 2.2 The SAURON data

The SAURON integral-field spectrograph (Integral Field Unit, hereafter IFU) has been extensively used at the Cassegrain focus of the William Herschel Telescope since 1999 (Bacon et al. 2001). All observations were conducted using the low spatial resolution mode which provides a field of view of about  $33'' \times 41''$  and a spatial sampling of  $0''.94 \times 0''.94$ . The narrow spectral range allows the user to probe a few stellar absorption and ionised gas emission lines with a spectral resolution of about 4 Angströms (FWHM).

All data reduction was performed using the dedicated XSAURON software wrapped in a scripted pipeline. A set of 64 galaxies included in the ATLAS<sup>3D</sup> sample were observed prior

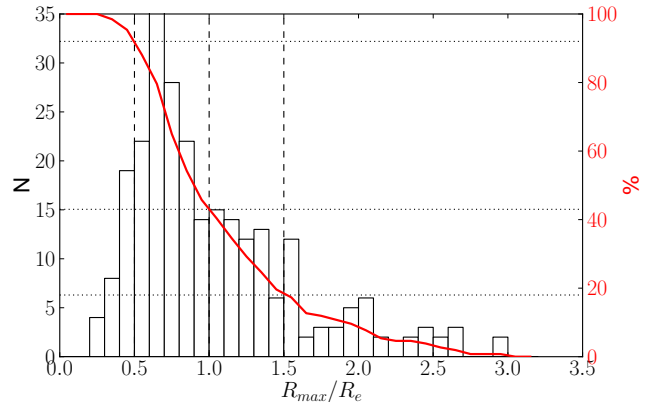


**Figure 1.** Histogram of the maximum aperture radius  $R_{max}$  covered by the SAURON observations of all 260 ATLAS<sup>3D</sup> galaxies (normalised by  $R_e$ ). The red line shows the corresponding cumulative function (right vertical scale) for galaxies with  $R > R_{max}$ : we cover about **92%, 43% and 18%** at  $R_e/2$ ,  $R_e$  and  $1.5 R_e$ , respectively, as indicated by the vertical/horizonal (dashed/dotted) lines.

to the mounting of the volume phase holographic (VPH) grating (mostly from the original SAURON survey, see de Zeeuw et al. 2002, for details). For these galaxies, we obtained an average of 2 hours on source sometimes following a mosaicing strategy to cover the targets with the largest effective radii. The spectral resolution attained for these galaxies is about 4.2 Angströms FWHM. For most of the 196 remaining targets, we integrated 1 hour on source centred on the object, including two (slightly dithered) 30mns exposures: only when the source was extended did we allow for a mosaic of 2 fields to attempt to fully cover the region within  $1 R_e$ , with two 30mns exposure for each field. The orientation of the SAURON field was adapted to each target to optimise the coverage of the galaxy taking into account its apparent photometric flattening. The spectral resolution attained for these 196 galaxies is about 10% better (due to the use of the VPH grating) and reaches 3.9 Angströms FWHM.

The 260 final merged datacubes (with  $0''.8 \times 0''.8$  rebinned spaxels) were then analysed using a common analysis pipeline, and using a minimum signal-to-noise threshold of 40 for the adaptive binning (Cappellari & Copin 2003). Gas and stellar kinematics were extracted via a pPXF algorithm (Cappellari & Emsellem 2004) with a library of stellar templates as in Emsellem et al. (2004), but adopting here the MILES library (Sánchez-Blázquez et al. 2006) and an optimised template per galaxy (see Paper I for details).

We derived  $\lambda_R$  and  $V/\sigma$  from growing effective apertures, as in E+07, following the ellipticity and position angle profiles obtained from the photometry, or from the constant values (kinematic axes and moment ellipticity from the outer part) for galaxies with obvious bars (see Sect. 2.1). Using two-dimensional spectroscopy, the expression for  $\lambda_R$  as given by:

$$\lambda_R \equiv \frac{\langle R |V| \rangle}{\langle R \sqrt{V^2 + \sigma^2} \rangle}, \quad (1)$$

transforms into

$$\lambda_R = \frac{\sum_{i=1}^{N_p} F_i R_i |V_i|}{\sum_{i=1}^{N_p} F_i R_i \sqrt{V_i^2 + \sigma_i^2}}, \quad (2)$$

where  $F_i$ ,  $R_i$ ,  $V_i$  and  $\sigma_i$  are the flux, circular radius, velocity and velocity dispersion of the  $i^{th}$  spatial bin, the sum running on the  $N_p$  bins. Considering the signal-to-noise threshold used here, we

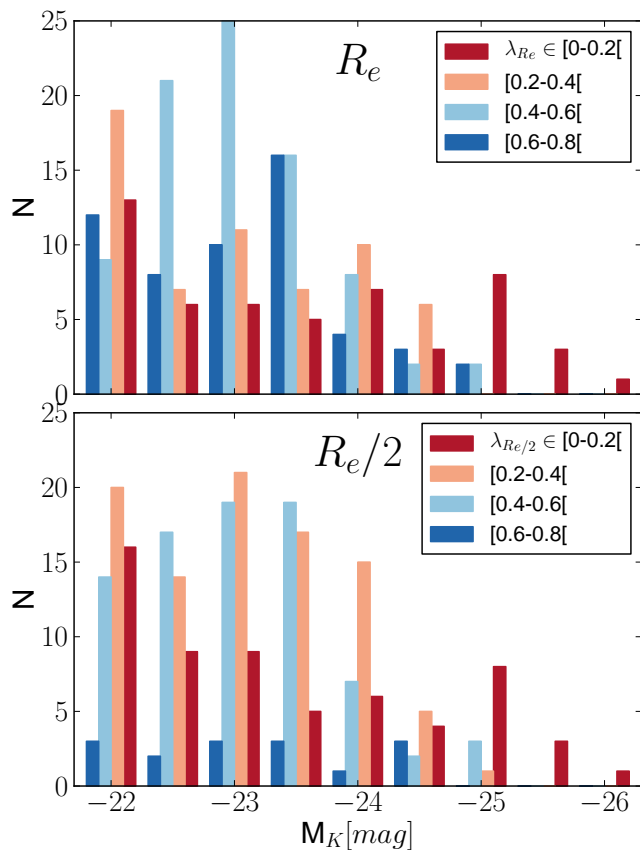


**Figure 2.** Histograms of K band luminosities for all 260 ATLAS<sup>3D</sup> galaxies, in bins of  $\lambda_{R_e}$  (red : [0 – 0.2]; light red : [0.2 – 0.4]; light blue : [0.4 – 0.6]; blue : [0.6 – 0.8]). The top panel uses  $\lambda_R$  values derived for an aperture radius of  $1 R_e$ , the bottom panel for an aperture radius of  $R_e/2$ .

expect a typical positive bias for values of  $\lambda_R$  near zero (see Appendix A of E+07) in the range [0.025– 0.05].

In the following, we will use  $\lambda_{R_e}$  and  $(V/\sigma)_e$  to denote values measured at  $1 R_e$ , and  $\lambda_{R_e/2}$  and  $(V/\sigma)_{e/2}$  for values at  $R_e/2$ . In Fig. 1, we provide an histogram of the maximum available effective aperture sizes from our SAURON dataset for the ATLAS<sup>3D</sup> sample: **we cover an aperture of at  $1 R_e$  or larger for 43% of our sample and  $R_e/2$  for 92% of all ATLAS<sup>3D</sup> galaxies. Note that 18% are covered up to at least  $1.5 R_e$ .**

Finally, accurate dynamical masses  $M_{\text{dyn}}$  were derived via Multi-Gaussian Expansion (Emsellem et al. 1994) of the galaxies’ photometry followed by detailed Jeans anisotropic dynamical models (Cappellari 2008; Scott et al. 2009) of the ATLAS<sup>3D</sup> SAURON stellar kinematics (Cappellari et al. 2010). This mass represents  $M_{\text{dyn}} \approx 2 \times M_{1/2}$ , where  $M_{1/2}$  is the total dynamical mass within a sphere containing half of the galaxy light.

### 3 A FIRST LOOK AT THE APPARENT ANGULAR MOMENTUM OF ATLAS<sup>3D</sup> GALAXIES

#### 3.1 Velocity structures and $\lambda_R$

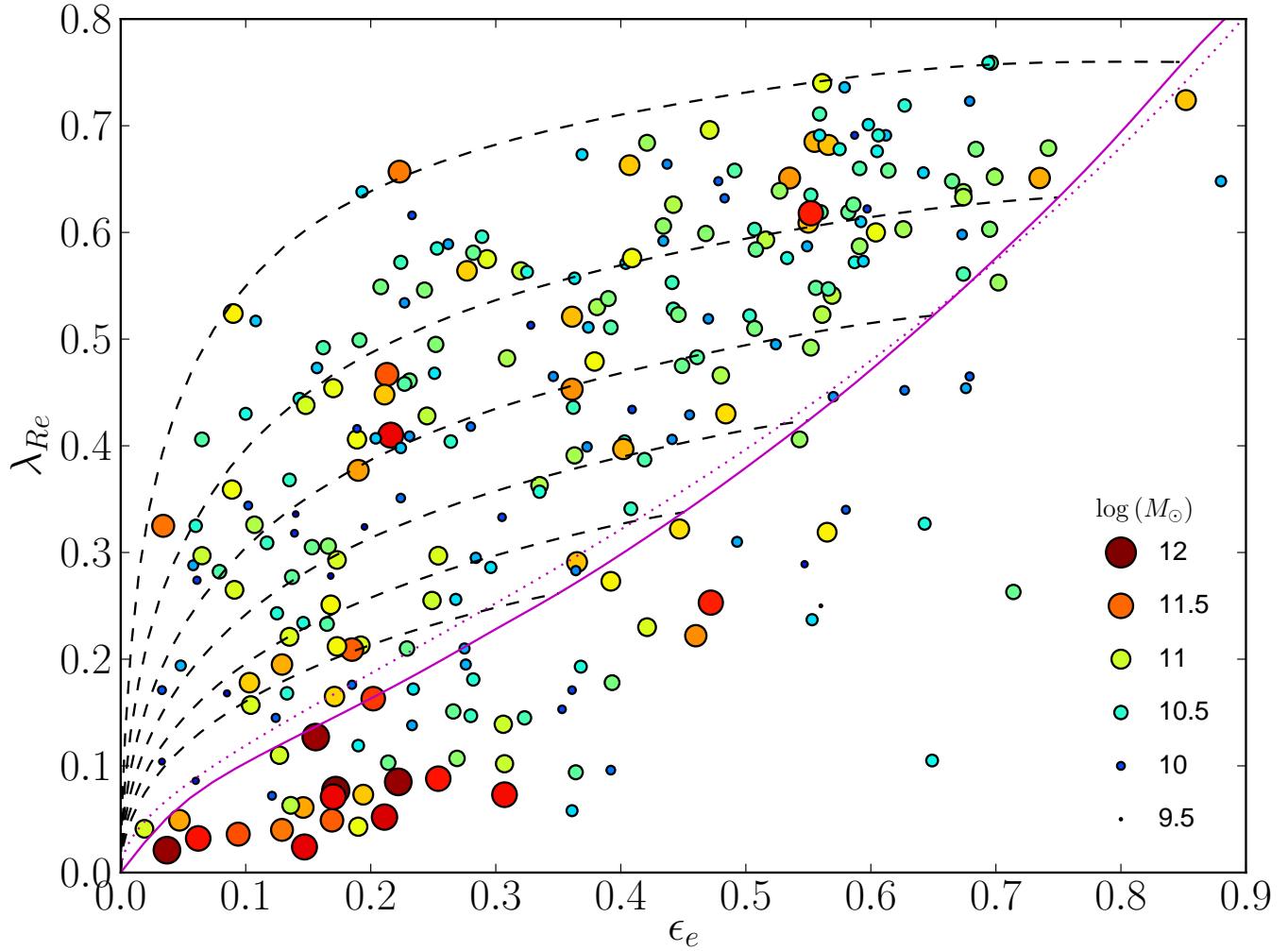
With the 260 stellar velocity maps from the ATLAS<sup>3D</sup> sample, we probe the whole range of velocity structures already uncovered by E+07: regular disc-like velocity fields (e.g., NGC 4452, NGC 3530), kinematically distinct cores (e.g., NGC 5481,

NGC 5631) or counter-rotating systems (NGC 661, NGC 3796), twisted velocity contours (e.g., NGC 3457, NGC 4552), sometimes due to the presence of a bar (e.g., IC 676, NGC 936). We also observe a few more galaxies with two large-scale counter-rotating disc-like components, as in NGC 4550 (Rubin et al. 1992), e.g., IC 0719 or NGC 448. IC 719 exhibits in fact two velocity sign changes along its major-axis, and NGC 4528 three sign changes. Only a few galaxies have noisy maps or suffer from systematics, e.g., NGC 1222, UGC 3960, or PGC 170172, due to the low signal to noise ratio of the associated datacubes or from intervening structures (e.g., stars). The reader is referred to Paper II for further details on the kinematic structures present in galaxies of the ATLAS<sup>3D</sup> sample.

The ATLAS<sup>3D</sup> sample of ETGs cover  $\lambda_{R_e}$  values from 0.021, with M87 (NGC 4486), therefore consistent with zero apparent angular momentum within the SAURON field of view, and 0.76 for NGC 5475 a flattened disc-like galaxy. Other galaxies with low  $\lambda_{R_e}$  values and stellar velocity fields with nearly zero velocity amplitude (within the noise level) are NGC 3073, NGC 4374, NGC 4636, NGC 4733, NGC 5846, and NGC 6703. Of these six, NGC 4374, NGC 4636, and NGC 5846 are nearly round, massive galaxies with a mass well above  $10^{11} M_{\odot}$ , and strong X-ray emitters. NGC 4636 shows a very low amplitude velocity field and a barely detectable kinematically distinct component. There are two more galaxies with significantly non-zero values of  $\lambda_{R_e}$  ( $\sim 0.1$ ) but no detectable rotation, the relatively high  $\lambda_{R_e}$  values being due to larger uncertainties in the kinematics: NGC 3073 and NGC 4733. Along with NGC 6703, these stand out as galaxies with no apparent rotation, a mass below  $10^{11} M_{\odot}$  and an effective radius smaller than 3 kpc: these are very probably nearly face-on disc-galaxies (NGC 4733 being a face-on barred galaxy).

If we use the previously defined threshold separating Slow and Fast Rotators, namely  $\lambda_{R_e} = 0.1$ , we count a total of 23 galaxies below that limit in our sample, a mere 9% of the full ATLAS<sup>3D</sup> sample. This is to be compared with one fourth (25%) of galaxies below that threshold found in E+07 within the representative SAURON sample of 48 early-type galaxies (de Zeeuw et al. 2002). With ATLAS<sup>3D</sup> we are covering a complete volume-limited sample, more than five times larger than the original SAURON sample, but we less than double the number of such slowly rotating objects. This is expected considering that such galaxies tend to be on the high luminosity end (E+07, C+07). A volume-limited sample includes far more galaxies in the low-luminosity range than the SAURON representative sample which had a flat luminosity distribution. Our ATLAS<sup>3D</sup> observations confirm the fact that slow and fast rotators are not distributed evenly in absolute magnitude: fast-rotating systems brighter than  $M_K$  of -24 are rare, while a third of all galaxies having  $\lambda_{R_e} \leq 0.1$  are in this range. This is emphasised in Fig. 2 where the K band luminosity histograms for galaxies in bins of  $\lambda_{R_e}$  are presented. This trend could be due to an incomplete field coverage of the brighter galaxies with large  $R_e$  when  $\lambda_R$  increases outwards (we reach  $1 R_e$  for only about 42%, see Fig. 1, and this is obviously biased toward the fainter end of galaxies), However, this trend is still present when using  $\lambda_R$  at  $R_e/2$  (bottom panel of Fig. 2) for which we have about 92% of all galaxies properly covered.

Among the 23 galaxies with  $\lambda_{R_e} \leq 0.1$  in the ATLAS<sup>3D</sup> sample, 6 have no detected rotation (3 of them being very probably face-on disc-like systems, see above), 2 have twisted or prolate-like isovelocity contours (NGC 4552 and NGC 4261), and out of the remaining 15 others, 14 have Kinematically Distinct Cores (KDCs,

6 *Eric Emsellem et al.*

**Figure 3.**  $\lambda_{R_e}$  versus ellipticity  $\epsilon_e$  for all 260 ATLAS<sup>3D</sup> galaxies. The colour and size of the symbols are associated with the mass of each galaxy, as indicated at the bottom right of the panel. The dotted magenta line show the edge-on view for elliptical galaxies integrated up to infinity with  $\beta = 0.70 \times \epsilon$ , as in C+07. The solid magenta line is the corresponding curve restricted to an aperture at  $1 R_e$  and for  $\beta = 0.65 \times \epsilon$  (see text for details). The black dashed lines correspond to the location of galaxies with intrinsic ellipticities  $\epsilon_{intr} = 0.85, 0.75, 0.65, 0.55, 0.45, 0.35$  along the relation given for an aperture of  $1 R_e$  with the viewing angle going from edge-on (on the relation) to face-on (towards the origin).

see Paper II), confirming the claim made in E+07 that most ETGs with low  $\lambda_R$  values have KDCs.

### 3.2 ATLAS<sup>3D</sup> galaxies in a $\lambda_R$ - $\epsilon$ diagram

The combination of the measured  $\lambda_{R_e}$  values with the apparent flattening  $\epsilon_e$  holds important clues pertaining to the intrinsic morphology and dynamics of ETGs, as shown in E+07. In Fig. 3, we provide a first glimpse at the distribution of galaxies in such a  $\lambda_R$ - $\epsilon$  diagram for an aperture radius of  $1 R_e$ .

A more standard approach includes the use of  $(V/\sigma)$  as a probe for the stellar kinematics of galaxies. In C+07, it has been shown that there seems to be a broad trend between the anisotropy of ETGs, parameterized<sup>1</sup> with  $\beta$ , and their intrinsic (edge-on) ellipticity  $\epsilon_{intr}$ . Fast rotators were found to be generally distributed

on the  $(V/\sigma)$ - $\epsilon$  diagram within the envelope traced by the edge-on relation  $\beta = 0.7 \times \epsilon_{intr}$  (from the analytic formula of Binney (2005)) and by its variation with inclination (Fig. 11 of C+07). This analytic relation is nearly identical to the one  $\beta = 0.65$ , which includes aperture integration within  $1 R_e$  (Appendix B). Since  $V/\sigma$  and  $\lambda_R$  of simple elliptical systems (with constant anisotropy) can be linked via a relatively simple formula (see Appendix B), we can translate these  $\beta$ - $\epsilon_{intr}$  relations for  $\lambda_R$  and provide the corresponding curves in a  $\lambda_R$ - $\epsilon$  diagram. These relations are shown in Fig. 3 for edge-on galaxies (dashed and solid magenta lines) as well as the effect of inclination (dashed black lines, only for the relation integrated within  $1 R_e$ ).

We first confirm that most of the galaxies with  $\lambda_{R_e}$  values significantly above 0.1 are located above (or at the left) of the magenta line in Fig. 3. The dashed line at  $\epsilon_{intr} = 0.85$  also provides a convenient upper envelope of the galaxies in our sample. This beautifully confirms the predictions made in C+07, using only a small set of targets, and reveals important characteristics of the internal state of early-type galaxies, which will be further discussed in Sect. 5.1.

The majority of galaxies above the magenta line are consis-

<sup>1</sup>  $\beta$  is the anisotropy parameter simply defined as  $1 - \sigma_z^2/\sigma_R^2$  for a steady-state system where  $\sigma_{R,z}$  are the cylindrical components of the stellar velocity dispersion.

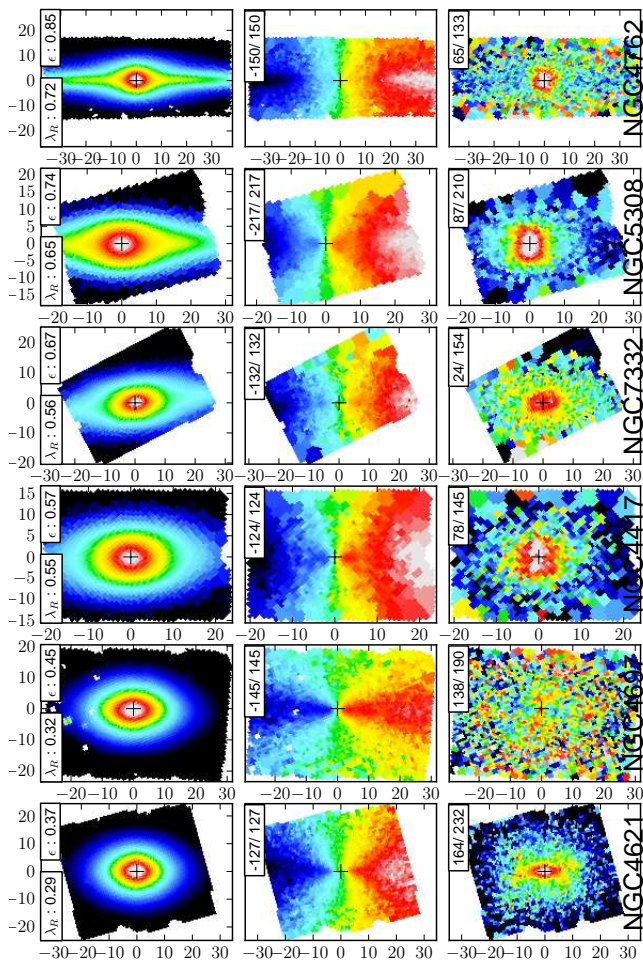


**Figure 4.** Reconstructed images and first two stellar velocity moment maps (velocity and velocity dispersion) for 6 galaxies selected near the ellipticity-anisotropy relation (magenta line, see text). The apparent ellipticity is decreasing from top to bottom.

tent with intrinsic ellipticities between 0.55 and 0.85, with only very few galaxies below  $\epsilon_{intr} = 0.35$ . The stellar velocity maps of these fast rotating objects, illustrated in Fig. 4 with 6 examples of galaxies from low ( $\sim 0.35$ , bottom), to high ( $\sim 0.85$ , top) ellipticities along the magenta line, are regular and show disc-like signatures (e.g., pinched isovelocity contours), strongly contrasting with the complex kinematic features observed for galaxies with low  $\lambda_{Re}$  values, as discussed in Sect. 3.1: this is objectively quantified in Paper II. We here probe from very flattened edge-on cases dominated by a thin disc component at the top, to relatively fatter objects like NGC 4621 at the bottom. All 6 galaxies exhibit a clear sign of a disc-like component either from flattened isophotes and/or pinched iso-velocities, confirming the fact that they cannot be viewed far from edge-on.

The distribution of galaxies in the ATLAS<sup>3D</sup> sample in the  $\lambda_R$ - $\epsilon$  plane also reveals a rather well-defined upper envelope: as ellipticity decreases, the maximum apparent angular momentum decreases accordingly. It can be understood by looking at Fig. 3 again where the upper black dashed line, corresponds to an extremely flattened spheroid with  $\epsilon_{intr} = 0.85$  (a disc) and an anisotropy parameter of  $\beta = 0.55$  (following the  $\beta$ - $\epsilon_{intr}$  relation mentioned above): most galaxies in the ATLAS<sup>3D</sup> sample have lower  $\lambda_R$ .

This first view at the distribution of the ATLAS<sup>3D</sup> galaxies in a

$\lambda_R$ - $\epsilon$  diagram provides a very significant upgrade on already published samples. We can therefore now proceed by combining the detailed study of the kinematic structures observed in these galaxies conducted in Paper II with such information to deliver a refined criterion for disentangling Fast and Slow Rotators.

## 4 GALAXY CLASSIFICATION VIA STELLAR KINEMATICS

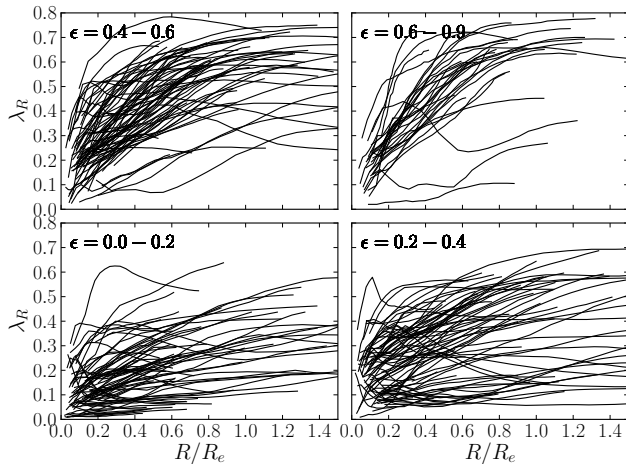
### 4.1 The importance of shapes

We have seen in the previous Section that galaxies with the lowest  $\lambda_R$  values tend to be more luminous or massive (see Figs. 2 and 3), and exhibit complex kinematic structures, as opposed to fast-rotating galaxies with regular velocity fields and disc-like signatures (when viewed near edge-on). This confirms the view delineated in E+07 and C+07, where early-type systems were separated into two families, the so-called Fast and Slow Rotators. However, it is not clear whether a *constant* value of  $\lambda_R$  (e.g.,  $\lambda_R = 0.1$  as defined in E+07 from a representative sample of 48 galaxies) corresponds to the best proxy for distinguishing between slow and fast rotators.

Using the complete ATLAS<sup>3D</sup> sample of 260 galaxies, we can in fact proceed with an improved criterion, taking into account the fact that two galaxies with the same apparent angular momentum but very different (intrinsic) flattening must have, by definition, a different orbital structure. A galaxy with a relatively low value of  $\lambda_R$ , e.g., of 0.2, may be consistent with a simple spheroidal axisymmetric system viewed at a high inclination (near face-on), but this is true only if its ellipticity is correspondingly low: a large ellipticity, e.g.,  $\epsilon = 0.4$ , would imply a more extreme object (in terms of orbital structure or anisotropy), as shown with the spheroidal models provided in Appendix B.

This can be further illustrated by looking at Fig. 5 where the radial  $\lambda_R$  profiles are shown for all galaxies of the sample in bins of ellipticities. For low ellipticities,  $0 < \epsilon < 0.2$ , there is a rather continuous sequence of profiles with various  $\lambda_R$  amplitudes from 0.1 to 0.5 at  $1 R_e$ : a rather face-on flattened system would have a profile similar to an inclined mildly-triaxial galaxy. In the next bin of ellipticities,  $0.2 < \epsilon < 0.4$ , we start discerning two main groups of galaxies: the ones with rapidly increasing  $\lambda_R$  profiles, most of these galaxies showing regular and symmetric velocity fields (as in Fig. 4), and those who have flatter (or even decreasing) profiles up to  $\sim R_e/2$  and then start increasing outwards, again often exhibiting complex velocity maps and distinct central stellar velocity structures. There are in addition a few galaxies with  $\lambda_R$  profiles going up to  $\sim 0.3$  and *decreasing* between  $R_e/2$  and  $R_e$ . As we reach the last ellipticity bin (with the highest values), most galaxies have strongly rising  $\lambda_R$  profiles reaching typical values of  $\lambda_R \sim 0.5$  at  $R_e/2$ . The 3 galaxies which have  $\lambda_{Re}$  below 0.4 are IC 719, NGC 448 and the famous NGC 4550, all being extreme examples of disc galaxies with two counter-rotating systems.

A refined scheme to separate slowly and fast rotating galaxies should therefore take into account the associated apparent ellipticity: we should expect a higher value of the specific stellar angular momentum for galaxies which are more flattened or closer to edge-on if these are all intrinsically fast rotators. Very flattened galaxies with  $\lambda_{Re}$  as low as 0.2 or 0.3 must already have a rather extreme orbital distribution (or strong anisotropy, see Appendix B). In the next Section, we use the completeness of our sample of early-type galaxies to revisit the question of how to distinguish members of

8 *Eric Emsellem et al.*

**Figure 5.**  $\lambda_R$  profiles for the complete ATLAS<sup>3D</sup> sample of early-type galaxies, in four bins of ellipticities  $\epsilon_e$  (as indicated in each panel), as a function of the aperture radius (relative to the effective radius  $R_e$ ).

the two main families of early-type galaxies, namely Slow and Fast Rotators.

#### 4.2 Kinematic structures and the link with $\lambda_R$

The classification of ETGs in Slow and Fast rotators was motivated by the (qualitative) realisation that galaxies within the SAURON sample of 48 ETGs (de Zeeuw et al. 2002) exhibit either regular stellar rotation, showing up as classical “spider-diagrams”, with no significant misalignment between the kinematic and photometric axes (excluding the few systems consistent with having no apparent rotation at all), or complex/irregular stellar velocity maps with twists and strong misalignment with respect to the photometry (Emsellem et al. 2004; Krajnović et al. 2008). Using  $\lambda_R$  as a proxy to disentangle the two families of objects, it was confirmed that these two families had distinct structural and dynamical properties (E+07, C+07).

We can now review these results in the context of our complete ATLAS<sup>3D</sup> sample: this requires an objective assessment of the observed kinematic structures. The regularity or richness of a velocity map can be defined and more importantly quantified using kinemetry (Krajnović et al. 2006). Such an evaluation has thus been conducted in Paper II systematically for all 260 ATLAS<sup>3D</sup> galaxies. The (normalised) amplitude of the 5<sup>th</sup> harmonic kinematic term  $k_5$  ( $k_5/k_1$ ) can for example be used to find out whether or not a velocity field has iso-velocity contours consistent (in azimuth) with the cosine law expected from pure disc rotation. The fact that the velocity map of a galaxy follows the cosine law does not directly imply that it is a pure-disc system, only that its line-of-sight velocity field looks similar to one of a two-dimensional disc. Using a threshold of 4% for  $k_5/k_1$ , galaxies with or without regular velocity patterns have been labelled in Paper II as Regular and Non-Regular Rotators, respectively, and provided a detailed and quantified account of observed velocity structures. Galaxies such as NGC 3379 or NGC 524 exhibit low amplitude rotation but are consistent with being regular rotators, while galaxies like NGC 4406 or NGC 4552 are clearly non-regular rotators (see Fig. B1, B5 and B6 of Paper II) even though these are rather round in projection.

All 260 galaxies of the ATLAS<sup>3D</sup> sample are shown with symbols for regular and non-regular rotators in Fig. 6: we plot both

measured  $V/\sigma_e$  and  $\lambda_{R_e}$  as functions of  $\epsilon_e$ . The expected locations for systems with  $\beta = 0.7 \times \epsilon$ , where  $\beta$  is the anisotropy parameter are presented as dotted lines, the magenta line representing edge-on systems and the dashed black line showing the effect of inclination for an intrinsic (edge-on) ellipticity of 0.82. These curves are calculated following the formalism in Binney (2005), and the specific values are identical to the ones defined in C+07. We also provide similar relations for  $\beta = 0.65 \times \epsilon$  as in Fig. 3, but this time taking into account the effect of a limited aperture ( $1 R_e$ ).

We observe in Fig. 6 that regular rotators tend to have  $V/\sigma$  or  $\lambda_R$  values above the magenta line. This clearly confirms the trend emphasised in C+07 already obtained with a significantly smaller sample. The ATLAS<sup>3D</sup> sample clearly extends this result to galaxies at higher ellipticities and  $V/\sigma$  or  $\lambda_R$  values. The second obvious and complementary fact is that non-regular rotators cluster in the lower part of the diagrams, and below the magenta line. Overall, this shows that objects with or without specific kinematic features in their velocity or dispersion maps tend to be distributed on either side of the relation illustrated by the magenta line.

This strongly suggests that the regularity of the stellar velocity pattern are closely related to the Slow and Fast rotators classes, as defined in E+07, and that the ATLAS<sup>3D</sup> sample of 260 galaxies provides the first view of a complete sample of ETGs, expanding on the perspective derived from the original SAURON sample of 48 galaxies. We do not expect a one to one relation between non-regular rotators and Slow rotators on one hand, and regular rotators and fast rotators on the other hand, because e.g., any departure from a regular disc-like rotation automatically qualifies a galaxy as a non-regular rotation pattern. However, apart from atypical cases such as unrelaxed merger remnants or galaxies with strong dust features, we may expect that such a link holds. We now examine how to best separate these two families of ETGs.

#### 4.3 Slow and Fast rotators

The  $V/\sigma$  diagram (Fig. 6) shows, independently from any refined criterion to disentangle regular and non-regular rotators, significantly higher overlap between the two populations both at low and high ellipticities. **The difference between  $V/\sigma$  and  $\lambda_R$  may not, however, be that obvious just looking at Fig. 6. For simple oblate models, as illustrated in Appendix B, there is a tight correlation between these two quantities (see Fig. B1). This is not the case anymore when the galaxy exhibits more complex kinematics, with e.g. a rapidly rotating inner part and a slowly-rotating outer part. Two galaxies with apparent dynamics as different as NGC 5813 and NGC 3379 have similar  $V/\sigma$  values, although the latter is a regular rotator while the former is a non-regular rotator with a clear stellar KDC (see E+07). In this context,  $\lambda_R$  is a better discriminant and this occurs because the weighting of stellar rotation depends both on the observed flux and on the size (radius) of the structure. While the difference may not be dramatic and would not impact the majority of ETGs (since most have regular stellar velocity fields), it becomes relevant when considering classes of galaxies for which we observe differences in the observed kinematic features. This has motivated the use of  $\lambda_R$  which also directly relates to the apparent angular momentum of the stars (E+07).**

Before we refine the above-mentioned criterion, we need to emphasise again the clear trend observed in the  $\lambda_R$ - $\epsilon$  diagram (bottom panel of Fig. 6): galaxies have on average increasing values of  $\lambda_R$  as the ellipticity increases, and this is valid also for non-regular rotators alone. As mentioned in Sect 4.1, at constant  $\lambda_R$  value, the

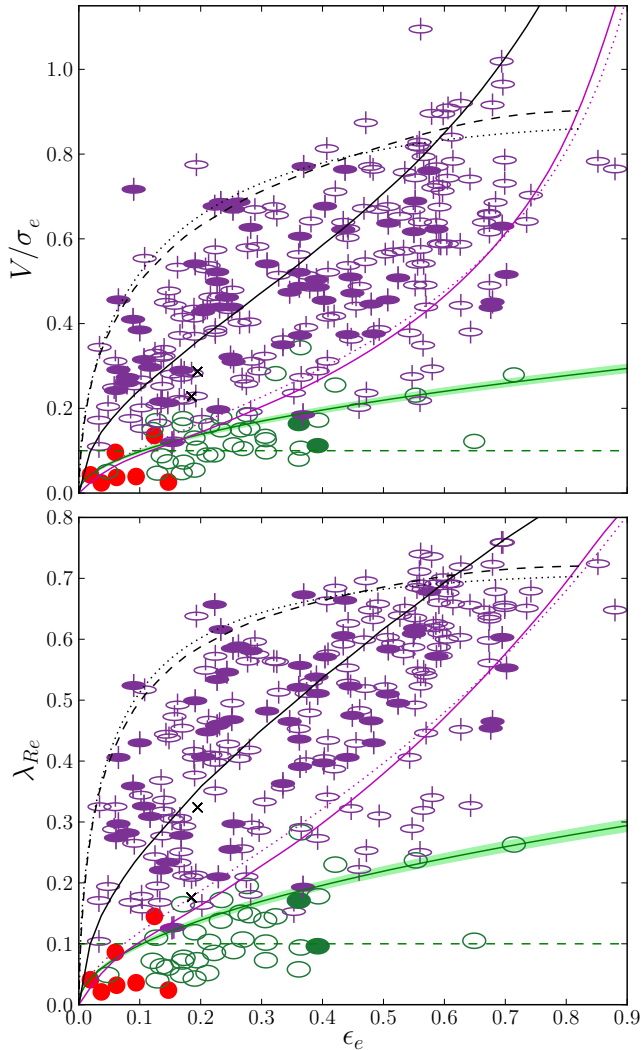


**Figure 6.** Measured  $V/\sigma_e$  (top) and  $\lambda_{Re}$  (bottom) values versus the ellipticity  $\epsilon_e$  within an aperture of  $1 R_e$ . The magenta lines are as in Fig. 3, and the black dotted and dashed lines represent the location of galaxies with an intrinsic ellipticity  $\epsilon = 0.82$  when going from an edge-on to a face-on view. The solid black line corresponds to isotropic oblate systems viewed edge-on. The solid green line is  $0.31 \times \sqrt{\epsilon}$ . Red circles are galaxies with no apparent rotation, green ellipses and purple symbols are for non-regular rotators and regular rotators, respectively. Filled symbols correspond to galaxies with bars. Regular and non-regular rotators are better separated using  $\lambda_R$  than  $V/\sigma$ .

anisotropy increases with higher ellipticities, and we therefore need to define a threshold for slow/fast rotators which depends on and increases with ellipticity.

We considered several possibilities, including scaled-down versions of the predicted  $\lambda_R - \epsilon$  relation for isotropic axisymmetric systems or of the magenta lines. The first one (isotropy being used as a reference) does a reasonable job at separating regular and non-regular rotators, with a scaling factor of  $\sim 0.4$  and would naturally connect our study with already published work. The fact that galaxies with low  $V/\sigma$  or  $\lambda_R$  exhibit different observed properties is certainly not a new result, and was illustrated and emphasised in a number of key studies (e.g., Bender 1988; Kormendy & Bender 1996) using the ratio  $V/\sigma_*$  between the measured  $V/\sigma$  and the predicted value from an oblate isotropic rotator  $V/\sigma_{iso}$  (see

e.g. Davies et al. 1983).  $V/\sigma_*$  has thus sometimes been used as an indication of an anisotropic dispersion tensor: this view is in fact misleading as a constant value for  $V/\sigma_*$  does imply an increasing anisotropy with increasing flattening (C+07). This statement is also valid for  $\lambda_{R*} = \lambda_R/\lambda_{Riso}$  obviously for the same reason.

More importantly, C+07 have shown that galaxies can generally not be considered as isotropic (see Fig. 6). Global anisotropy increases with the intrinsic flattening, therefore using isotropic rotators as a reference for flattened galaxies would not be appropriate. Galaxies in the ATLAS<sup>3D</sup> sample appear to be distributed around the isotropy line in Fig. 6, but this relation is derived for *edge-on* systems, and galaxies should span the full range of inclinations with roughly as many galaxies above and below an inclination of  $60^\circ$ . Scaling of the magenta line would in this context be more appropriate, although it clearly has a similar drawback: it is defined for intrinsically edge-on systems, does not follow the variation of  $\lambda_R$  and  $\epsilon$  due to inclination effects, and therefore does not perform well in disentangling regular rotators from non-regular ones.

After considering various possibilities, we finally converged on what we believe is the simplest proxy which can properly account for the two observed families, minimising the contamination on both sides. We therefore fixed the threshold for  $\lambda_R$  to be proportional to  $\sqrt{\epsilon}$  with a scaling parameter  $k_{FS}$  which depends on the considered apertures, namely:

$$\lambda_{Re} = (0.31 \pm 0.01) \times \sqrt{\epsilon_e} \quad (3)$$

$$\lambda_{Re/2} = (0.265 \pm 0.01) \times \sqrt{\epsilon_e/2} \quad (4)$$

The different values of  $k_{FS}$  for these two apertures obviously follow the observed mean ratio between  $\lambda_{Re}$  and  $\lambda_{Re/2}$  (see Appendix B). Here,  $\lambda_R$  and  $\epsilon$  are *measured* values: formal errors for these are very small (because these parameters are computed using many independent spaxels). Uncertainties in the measurements of  $\lambda_R$  are thus mostly affected by systematic errors in the stellar kinematic values and are difficult to assess. The quoted ranges in Eqs. 3 and 4 ( $[0.30 - 0.32]$  and  $[0.255 - 0.275]$  for  $R_e$  and  $R_e/2$ , respectively) are therefore only indicative of the difficulty in defining such empirical thresholds. The relation for an  $1 R_e$  aperture is shown as a solid green line (the filled area showing the quoted ranges) in Fig. 6: it performs well in its role to separate galaxies with regular and non-regular velocity patterns, and does slightly better with  $\lambda_R$  than with  $V/\sigma$  which shows a 50% increase of misclassified objects (and a larger number of non-regular rotators above the magenta line). The two non-rotators which are above the green line (NGC 3073 and NGC 4733; red circles) are in fact very probably face-on fast-rotating galaxies.

Equations 3 and 4 can therefore be used to define Fast and Slow rotators, but as for any classification scheme, we need to define a scale at which to apply the criteria: this is further examined in the next Section.

#### 4.4 The importance of a scale

Large-scale structures ( $\sim 2R_e$  and beyond) are certainly important to understand the formation and assembly history of galaxies, and reveal e.g., signatures such as faint tidal structures or streams. However, we are interested here in probing the central regions of early-type galaxies, at the depth of their potential wells where metals are expected to have accumulated or been produced, and where stellar structures should have had time to dynamically relax: using apertures of one effective radius follows these guidelines and, moreover, covers about 50% of the stellar mass.

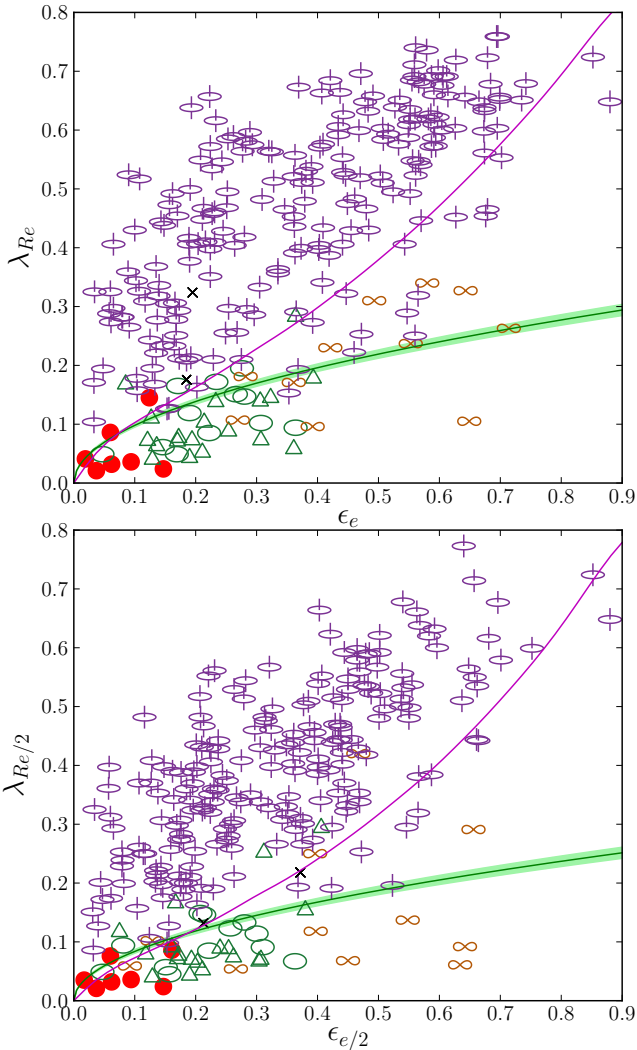


**Figure 7.** As in the bottom panel of Fig. 6, but here for  $\lambda_R$  within apertures of  $R_e$  (top panel) and  $R_e/2$  (bottom) panel. Symbols correspond to different kinematic groups (see text for details): red circles are non-rotators, green ellipses are for non-regular rotators without any specific kinematic feature, green triangles are galaxies with KDCs, orange lemniscates are  $2\sigma$  galaxies (galaxies with two counter-rotating flattened stellar components), purple symbols are regular rotators and black crosses are 2 galaxies which could not be classified.

Stellar angular momentum is generally observed to increase at large radii (E+07), even for slow rotators, and this is also valid for most ATLAS<sup>3D</sup> galaxies (Fig. 5). The majority of fast rotating galaxies reach close to their maximum  $\lambda_R$  values between  $R_e/2$  and  $R_e$ : beyond that radius, the profiles often smoothly bend and reach a plateau. Many galaxies with low central apparent angular momentum also show  $\lambda_{R_e}$  increasing values outside  $R_e/2$ . It is also true that most kinematically distinct components observed in our ATLAS<sup>3D</sup> sample have radii smaller than  $R_e/2$ . And for all the detected KDCs in our sample, the maximum radius covered is at least 50% larger than the radius of the KDC itself. This suggests that both apertures of  $R_e/2$  and  $R_e$  could serve as reference scales to define Slow and Fast Rotators (SRs and FRs, respectively). Using apertures smaller than  $R_e/2$  is not advised, as this would make the measurements more dependent on instrumental characteristics and observation conditions, and would probe only the core regions. To

compare how our criterion performs for  $1 R_e$  and  $R_e/2$ , we will use a more detailed description of the kinematic features present in the maps: this will help interpreting the observed similarities and differences.

In Paper II, the regular/non-regular rotator types, which globally define the observed velocity structure of a galaxy (in combination with key features observed in both the velocity *and* velocity dispersion maps and analysed via kinemetry), have been used to define five kinematic groups:

- *Group a*: galaxies with no apparent rotation, or non-rotators (7 members);
- *Group b*: galaxies with non regular velocity pattern (non-regular rotators) but without any specific kinematic feature (12 members);
- *Group c*: galaxies with Kinematically Distinct or Counter-rotating Cores (19 members);
- *Group d*: galaxies with two symmetrical off-centred stellar velocity dispersion peaks (11 members);
- *Group e*: galaxies with regular apparent rotation (regular rotators) and with or without small minor-axis kinematic twists (209 members).

Galaxies of groups *a* to *d* are mostly non-regular rotators, while most of the galaxies in group *e* are regular rotators. Galaxies of *group d*, also called ‘ $2\sigma$ ’ galaxies due to the appearance of their velocity dispersion maps, are interpreted as systems with two counter-rotating flattened stellar components which can have various relative luminosity contributions. This includes galaxies such as the well-known NGC 4550 (Rubin et al. 1992), which is made of two counter-rotating discs of nearly equal light (Rix et al. 1992, C+07), and for this reason ends up as a slow rotator, or other cases like NGC 4473, which has a smaller amount of counter-rotating stars (C+07) and thus appears as a fast rotator, or newly discovered objects like NGC 4528 (Paper II). Among our sample of 260 objects, two galaxies could not be classified due to the low signal-to-noise ratio of the extracted kinematics.

In Fig. 7, we now re-examine the  $\lambda_R$  values for our ATLAS<sup>3D</sup> sample in the light of these 5 *kinematic groups* for both apertures of  $R_e$  and  $R_e/2$ . As expected, both the ellipticity  $\epsilon$  and  $\lambda_R$  values are smaller within  $R_e/2$ :  $\lambda_R$  is generally an increasing function of radius and going inwards we tend to shift away from a large-scale disc structure when present (the median of our observed  $\lambda_{R_e}/\lambda_{R_e/2}$  values is  $\sim 1.17$ ; see also Appendix B). All results previously mentioned within an aperture of  $1 R_e$  are confirmed with a smaller one ( $R_e/2$ ). The galaxies of *kinematic groups a, b, c, d* seem to nicely cluster below the green lines defined in Eqs. 3 and 4, and the resulting separation of these targets from the *kinematic group e* (regular rotator) is marginally sharper within  $R_e/2$ : there are no galaxies of *group e* below the green line and most  $2\sigma$  galaxies are now below the defined threshold for slow rotators.

Eqs. 3 and 4 thus provide excellent (and simple) proxies to discriminate between galaxies of *kinematic groups a, b, c, d* and *group e*, or conversely between regular and non-regular rotators, with only one object with regular disc-like stellar velocity maps below the line (NGC 4476) at  $1 R_e$  and none for the smaller aperture. In fact, NGC 4476 seems to be a bona fide *group d* galaxy, but with an usually large inner counter-rotating component (Alison Crocker, priv. communication).

Using these criteria, there are 36 Slow Rotators (SRs) out of 260 for an aperture of  $R_e$  and 37 for  $R_e/2$ , with 30 in common for both apertures. All targets which change class going from  $R_e/2$  to  $R_e$  are well covered with the available SAURON field

of view, and this is therefore not an effect of spatial coverage. Galaxies which are FRs at  $R_e/2$  and SRs at  $R_e$  are NGC 4476, NGC 4528, NGC 5631, PGC 28887, UGC 3960 and those being SRs at  $R_e/2$  and FRs at  $R_e$  are IC 719, NGC 770, NGC 3073, NGC 3757, NGC 4259, NGC 4803, NGC 7710. All except two of these are either near the dividing line, or specific cases such as, again, NGC 4550-like systems. The two discrepant cases, namely NGC 4476 and PGC 28887, have central decoupled kinematic components with a radial size larger than  $R_e/2$ . The fact that  $2\sigma$  galaxies change class and that we still have some of them above the threshold even within  $R_e/2$  (NGC 448 and NGC 4473) is expected, as the corresponding counter-rotating components span a range of spatial extent and luminosity contribution which directly affect the  $\lambda_R$  measurements:  $2\sigma$  galaxies which are Slow Rotators have a high enough contribution within the considered aperture to significantly influence the measured stellar angular momentum.

As mentioned, 30 out of 36 SRs at  $R_e$  are also SRs at  $R_e/2$ : for 22 of these, the SAURON data does not reach  $1 R_e$ . Considering a simple extrapolation of their  $\lambda_R$  profiles (see also E+07), there is little chance that any of these cross the threshold between SRs and FRs at  $R_e$ . We therefore advocate the use of one effective radius  $R_e$  as the main scale to probe FRs and SRs, considering that doing so focuses the classification on a central but fixed and significant fraction (50%) of its luminosity.

By defining our classification criteria to such central regions, we may be weighting more towards dissipative processes, and consequently avoiding regions dominated by the dry assembly of galaxies (Khochfar & Burkert 2003) which is thought to mostly affect the outer parts (Naab et al. 2007, 2009; Hopkins et al. 2009b; Hoffman et al. 2010; Bois et al. 2010; Oser et al. 2010). We may also consequently miss very large KDCs (Coccatto et al. 2009) or e.g., any outer signature of interaction. This should obviously be kept in mind when interpreting the results: depending on the formation and assembly history, we expect galaxies to have significantly different radial distribution of their stellar angular momentum.

The use of an aperture radius of  $1 R_e$  is motivated by the following facts: it has **discriminating** power, as shown in the previous Section, and we expect differences to be apparent in simulations (see Sect. 5.3); such a scale is accessible to integral-field spectroscopy as well as modern numerical simulations; it is large enough that it should not significantly suffer from variations in the observational conditions (e.g., seeing); it traces a significant fraction of the stellar mass, namely about 50% for systems with shallow spatial variations of their stellar populations. We note here that we obtain consistent results with a smaller aperture,  $R_e/2$ , besides the change of class for a few flattened SRs from the  $2\sigma$  kinematic group. We acknowledge, however, that this consistency may not hold for arbitrarily large apertures, even though the criterion itself is a function of the aperture size.

Our refined criterion is motivated to respect the relation between dynamical structure and apparent shape, which should increase its robustness to e.g., changing rotation at different radii. We also note that the criterion itself is empirically determined, and changes depending on the scale used. One should avoid using the distribution measured at e.g.,  $R_e$ , to classify galaxies based on data from grossly different spatial scales. It is also critical for any comparison of simulations with observed galaxies to measure these parameters consistently, using the same spatial extent.

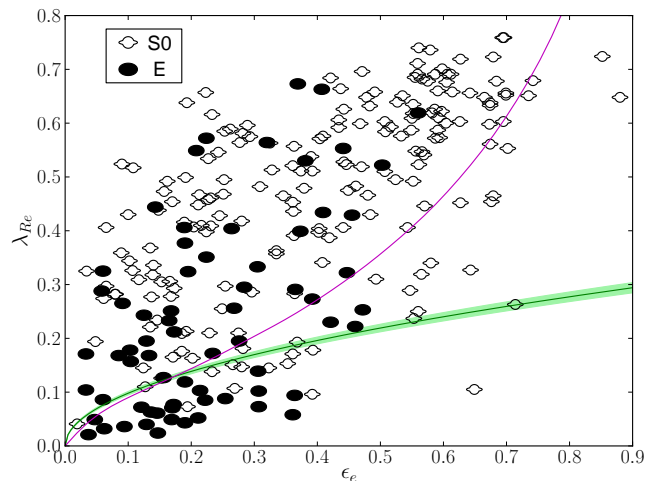


**Figure 8.**  $\lambda_{Re}$  versus the ellipticity  $\epsilon$  within an aperture of  $R_e$ . The lines are as in Fig. 7. The filled ellipses and open symbols are galaxies with a morphological type  $T < -3.5$  (E's, ellipticals) and  $T \geq -3.5$  (S0, lenticulars), respectively. Note the many E's which are Fast Rotators (above the green line).

#### 4.5 Robustness of the new classification scheme

The new proxy for Slow and Fast Rotators (SR and FR, respectively) differs from the previous constant threshold criterion in two main ways. Firstly, at high ellipticities it reaches higher  $\lambda_R$  values ( $\sim 0.25$  for  $\epsilon = 0.8$ ). Secondly, the new relation goes to zero for very low ellipticities (apparently round galaxies). The three non-rotators (red circles in Fig. 6) which are close to the defined relation are all very probably nearly face-on rapidly rotating galaxies which would be significantly above the line if they were viewed edge-on. For a Fast Rotator to be consistent with no rotation requires very low inclination and therefore extremely round isophotes (see e.g. Jesseit et al. 2009). The new relation works significantly better at disentangling such cases from the truly low angular momentum galaxies. This partly comes from the fact that the dependency on the ellipticity (criterion  $\propto \sqrt{\epsilon}$ ) somewhat mimics the variation of  $\lambda_R$  and  $\epsilon$  due to inclination effects.

The new criterion defined should minimise contamination and mis-classification, but as for any empirically designed classification, we expect some ambiguous cases, or systems for which it is hard to conclude. There are, for example, two galaxies, namely NGC 5173 and NGC 3757, which coincidentally have the same  $\lambda_{Re/2}$  and  $\epsilon_{e/2}$ , and lie at the very limit between SRs and FRs (NGC 3757 is in fact a galaxy with a bar which perturbs the ellipticity measurement). Three non-regular rotators are significantly above the curve (to be compared with the total of 224 Fast Rotators), namely NGC 770, NGC 5485, NGC 7465: NGC 770 is a galaxy with a known counter-rotating disc (Geha et al. 2005), NGC 5485 is one of the rare galaxies with prolate kinematics (as NGC 4621), and NGC 7465, which is the non-regular rotator with the highest  $\lambda_{Re}$  value, is an interacting system forming a pair with NGC 7464 (Li & Seaquist 1994) and shows a complex stellar velocity field with a misaligned central disc-like component.

The probability of a galaxy to be misclassified as a Slow (or Fast) Rotator is hard to assess. We can at least estimate the uncertainty on the number of Slow Rotators in our sample by using the uncertainty on the measurements themselves ( $\lambda_R$  and  $\epsilon$ ), the observed distribution of points, and the intrinsic uncertainty in defining the threshold for  $\lambda_R^N = \lambda_R/\sqrt{\epsilon}$ . Using  $R_e$  as the refer-

## 12 *Eric Emsellem et al.*

ence aperture, we estimate the potential contamination of SRs by FRs by running Monte Carlo simulations on our sample (assuming gaussian distribution for the uncertainty on  $\epsilon$  and  $\lambda_R$  of 0.05) to be  $\pm 6$  galaxies ( $2\sigma$ ). We obtain a relative fraction of  $\sim 14 \pm 2\%$  of SRs in the full ATLAS<sup>3D</sup> sample of ETGs, which represents 4% of the full parent sample of 871 galaxies (Paper I). This is much lower than the 25% quoted in E+07, but as mentioned above, this is due to the flatness of the luminosity **distribution** of the original SAURON sample.

### 4.6 Slow, Fast Rotators, and Hubble types

We now examine the Hubble type classification in the light of our new scheme to separate Fast and Slow Rotators. In Fig. 8, we show the distribution of galaxies in the  $\lambda_R$ - $\epsilon$  diagram using the two main classes of “Ellipticals” or E’s ( $T < -3.5$ ) and “Lenticulars” or S0’s ( $T \geq -3.5$ , as defined in Paturel et al. 2003).

The ATLAS<sup>3D</sup> sample of 260 ETGs includes 192 S0’s and 68 E’s. As expected, E’s in the ATLAS<sup>3D</sup> sample tend on average to be more massive and rounder than S0’s. We therefore naturally retrieve the trend that E’s tend to populate the left part of the diagram, and within the SR class, there is a clear correlation between the apparent ellipticity and being classified as an E or S0, the latter being all more flattened than  $\epsilon = 0.2$ . Ellipticals also tend to be in the lower part of the diagram (low value of  $\lambda_R$ ), while the highest  $\lambda_R$  values correspond to S0 galaxies. Most Slow Rotators which are not  $2\sigma$  galaxies are classified as E’s (23/32).

As expected, the vast majority of galaxies with ellipticities  $\epsilon_e > 0.5$  are S0s. However, 20% of all Fast Rotators (45/224) are E’s, and 66% of all E’s in the ATLAS<sup>3D</sup> sample are Fast Rotators. Also the fact that all  $2\sigma$  galaxies except one (NGC 4473) are classified as S0’s demonstrate that global morphology alone is not sufficient to reveal the dynamical state of ETGs. **The E/S0 classification alone is obviously not a robust way to assess the dynamical state of a galaxy. There is in fact no clear correlation between  $\lambda_R/\sqrt{\epsilon}$  and the morphological type  $T$ , besides the trends mentioned here. From Fig. 8, we expect a significant fraction of galaxies classified as E’s to be inclined versions of systems which would be classified as S0s when edge-on, and just separating ETGs into Es and S0s is therefore misleading.**

### 4.7 Properties of Slow and Fast Rotators

The detailed distribution of galaxies in *groups a, b, c, d and e* as defined in Paper II is shown in Fig. 9 using histograms of  $\lambda_R^N = \lambda_R/\sqrt{\epsilon}$  values both for  $R_e$  and  $R_e/2$ . The *group e* galaxies, and consequently the Fast Rotators, peak at a value of around 0.75 within  $R_e/2$  and 0.85 for  $R_e$ . Slow Rotators are defined as galaxies with  $\lambda_R^N < k_{FS}$ , mostly associated with galaxies from *groups a to d*, which represent the lower tail of that distribution with some small overlap with the *group e*. **We provide the SAURON stellar velocity and velocity dispersion maps of all 36 Slow Rotators in Fig. A1 and A2 of Appendix A. We refer the reader to Krajević et al. (2011) for all other SAURON stellar velocity maps.**

We re-emphasise in Figs. 10 and 11 the trend for Slow Rotators to be on the high mass end of our sample. Slow Rotators span the full range of dynamical masses present in the ATLAS<sup>3D</sup> sample. However, most non-rotators and galaxies with KDCs have masses above  $10^{10.75} M_\odot$ . If we exclude the three potential face-on Fast Rotators (see Sect. 3), all non-rotators have masses above  $10^{11.25} M_\odot$ . These non-rotators and KDC galaxies clearly have

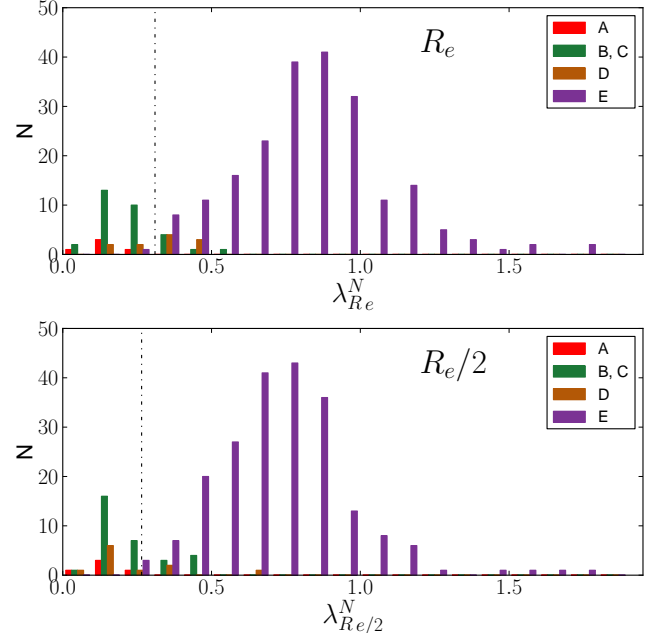


**Figure 9.** Histograms of galaxies in the ATLAS<sup>3D</sup> sample showing the distribution of  $\lambda_R^N = \lambda_R/\sqrt{\epsilon}$  within an aperture of  $R_e/2$  (top panel) and  $R_e$  (bottom panel) for non-rotators (A), featureless non-regular rotators with or without a KDC (B and C) in green,  $2\sigma$  galaxies (D) in orange, and non-regular rotators (E) in purple. The vertical dashed lines in each panel show the limit set (0.265 and 0.31, for  $R_e/2$  and  $R_e$ , respectively) between Slow and Fast Rotators for both apertures. To avoid confusion, we have excluded the two non-rotators, NGC 3703 and NGC 4733, which are assumed to be face-on fast rotators.

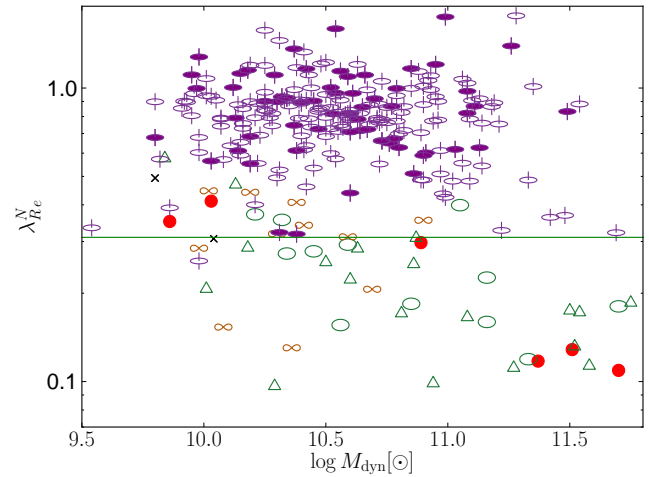


**Figure 10.**  $\lambda_{R_e}^N$  (log-scale) versus dynamical masses  $M_{\text{dyn}}$ . Symbols are as in Fig. 7. The horizontal green solid line indicates the limit between Fast and Slow Rotators.

a different mass distribution than  $2\sigma$  galaxies which are all, except NGC 4473, below  $10^{10.75} M_\odot$ . The normalised  $\lambda_{R_e}^N$  value for Slow Rotators tend to decrease with increasing mass (Fig. 10): the mean  $\lambda_{R_e}^N$  values for Slow Rotators below and above a mass of  $10^{11.25} M_\odot$  are about 0.22 and 0.13, respectively. Fast Rotators overall seem to be spread over all  $\lambda_{R_e}^N$  values up to a dynamical mass  $10^{11.25} M_\odot$  where we observe the most extreme instances of Slow Rotators (e.g., non-rotators). In Fig. 11 we show  $\epsilon_e$  with re-

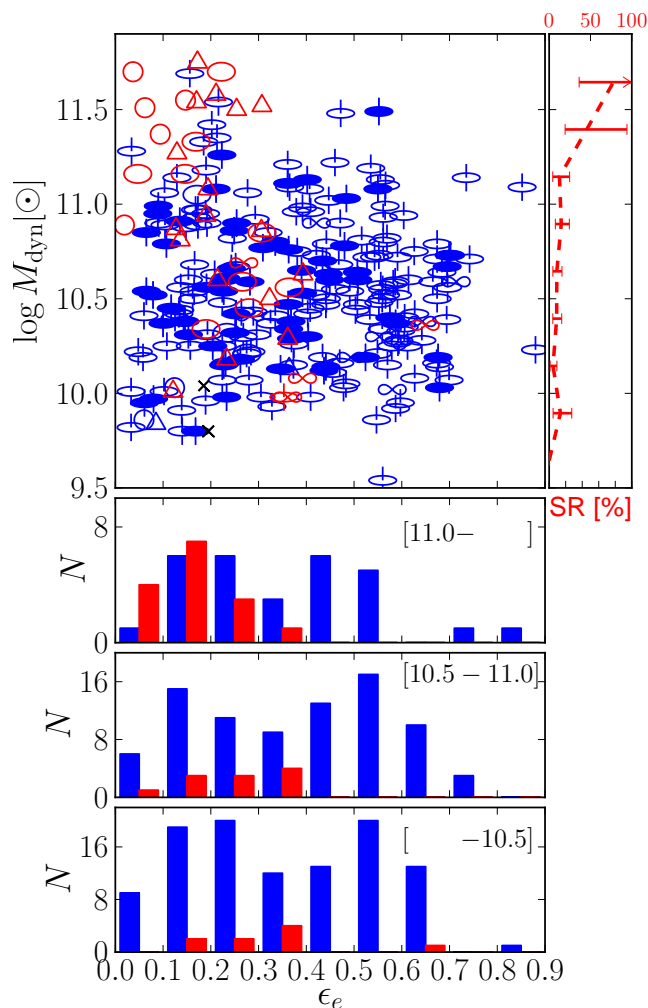


**Figure 11.** Dynamical masses  $M_{\text{dyn}}$  versus  $\epsilon_e$ . The top left panel shows the distribution of ATLAS<sup>3D</sup> galaxies with blue and red colours now correspond to Fast and Slow Rotators, respectively. Symbols are as in Fig. 7. The thick red dashed curve with errorbars on the top right panel shows the fraction of Slow Rotators (for  $1 R_e$ ) for mass bins with widths of 0.25 in  $\log M_{\text{dyn}}$  with the corresponding labels given on top x-axis. The three lower panels present the ellipticity within  $R_e$  histograms in bins of masses ( $\log M_{\text{dyn}}$ ), indicated in brackets in each sup-panel. Note the increased fraction of Slow Rotators in the 2 highest mass bins, and the shift of the ellipticity of Slow Rotators above and below  $10^{11} M_{\odot}$ .

spect to the dynamical mass  $M_{\text{dyn}}$  where we have coloured each symbol following the Fast (blue) and Slow (red) Rotator classes. Fig. 11 also shows the fraction of Slow Rotators with respect to the total number of galaxies within certain mass bins: Slow Rotators represent between 5 and 15% of all galaxies between  $10^{10}$  and  $10^{11.25} M_{\odot}$ . As already mentioned, above  $10^{11.25} M_{\odot}$  the fraction of Slow Rotators shoots up very significantly, reaching 45 and 77% in the last two mass bins below and above  $10^{11.5} M_{\odot}$ , respectively.

There is a tendency for Slow Rotators above  $10^{11} M_{\odot}$  to have rounder isophotes with ellipticities  $\epsilon_e$  between 0 and 0.3 and mostly below 0.2, while most Slow Rotators below  $10^{11} M_{\odot}$  have ellipticities distributed between 0.2 and 0.4 (Fig. 11). The weak trend for Slow rotators at higher mass to have lower  $\lambda_{R_e}^N$  could thus be associated with the corresponding ellipticity decrease. Fast Rotators seem to be smoothly distributed over the full range of ellipticities

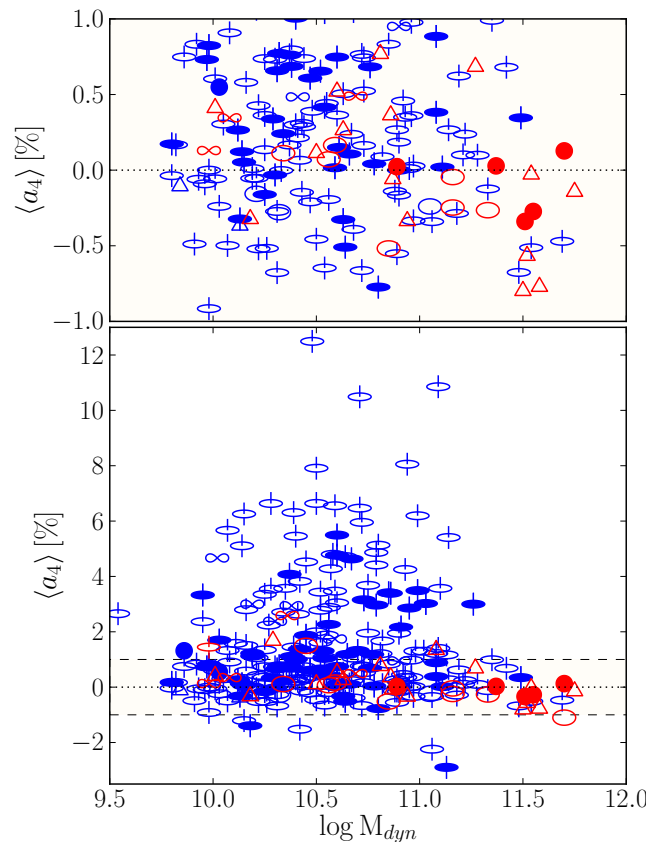


**Figure 12.** The averaged  $a_4$  (in % within  $1 R_e$ ) versus the dynamical mass for galaxies in the ATLAS<sup>3D</sup> sample. The top panel is a zoomed version of the bottom panel. The top panel shows the distribution of  $a_4$  values between  $-1$  and  $+1$ . Symbols are as in the top panel of Fig. 11.

between  $10^{9.75} M_{\odot}$ , near the lower mass (luminosity) cut of our sample, and  $10^{11.25} M_{\odot}$  above which Slow Rotators clearly dominate in numbers. All these results are also valid when using a smaller aperture ( $R_e/2$ ).

#### 4.8 Isophote shapes and central light profiles

Massive Slow Rotators have, as expected, slightly boxy isophotes, as shown in Figs. 12 where we present  $\langle a_4 \rangle$ , the luminosity weighted average of  $a_4$  within  $1 R_e$ , versus the dynamical mass. This is a known result, specifically emphasised by Kormendy & Bender (1996) who suggested the use of the  $a_4$  parameter, quantifying the degree of boxiness or disciness of the isophotes, to assess the dynamical status of early-type galaxies. All 9 galaxies within the ATLAS<sup>3D</sup> sample with masses larger than  $10^{11.5} M_{\odot}$  have  $a_4$  values which are negative or very close to zero, but these include 2 fast rotators, namely NGC 3665 and NGC 4649. In fact 70% of the Slow Rotators more massive than  $10^{11} M_{\odot}$  are boxy, while in the same mass range only 30% of the Fast Rotators are. Below a mass of  $10^{11} M_{\odot}$ , we observe the same overall fraction ( $\sim 25\%$ ) of boxy systems in both Slow and Fast Rotators. This means that the relative fraction of Fast Rotators which are boxy is nearly constant with mass, while there a drastic change of the boxiness/disciness in the population of Slow Rotators around a mass of  $10^{11} M_{\odot}$ . We also note that most discy Slow Rotators exhibit a KDC, or are  $2\sigma$  galaxies. Since all  $2\sigma$  galaxies are discy and the identification of

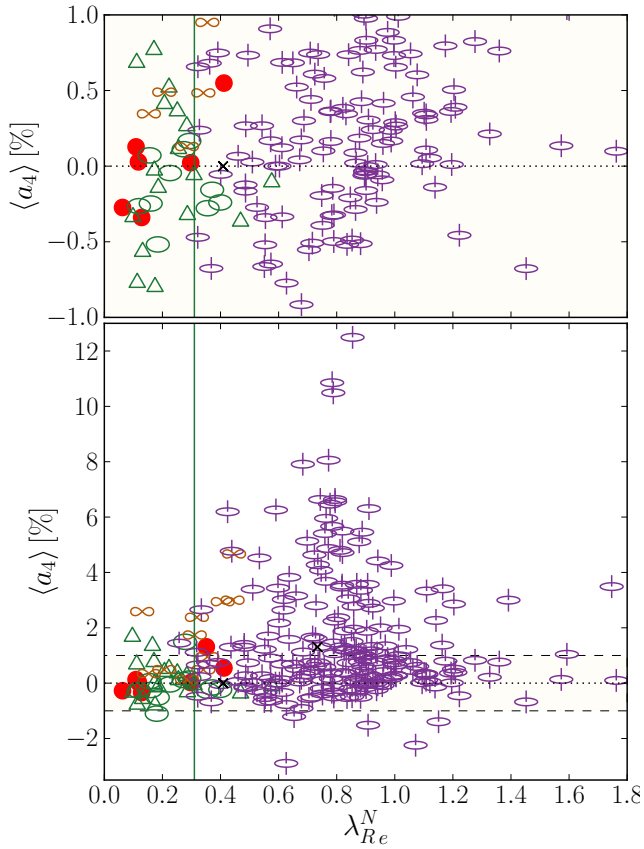


**Figure 13.**  $\lambda_{R_e}^N$  versus the averaged  $a_4$  (in % within  $1 R_e$ ). The top panel is a zoomed version of the bottom panel, including only  $a_4$  values between  $-1$  and  $+1$ . Symbols are as in Fig. 7. **The vertical green light represents the threshold between Slow and Fast Rotators, as defined in the present paper.**

such systems depends on the viewing angle, we should expect that some of these discy Slow Rotators are bona fide  $2\sigma$ : a confirmation of this hypothesis requires detailed modelling of the photometry and stellar kinematics.

In Fig. 13, we now show how  $\langle a_4 \rangle$  varies with the normalised value  $\lambda_{R_e}^N$  with the symbols of the different kinematic groups. Non regular rotators with no specific kinematic feature (*group b*) are more often boxy. Galaxies with KDCs (*group c*) can be both discy or boxy. Larger positive disciness values are reached for higher  $\lambda_R$  values as already emphasised in E+07, and galaxies with  $\langle a_4 \rangle$  larger than 3% are all Fast Rotators. A little more than 20% of all Fast Rotators are boxy (48/224), but most of them (32) with rather low absolute values (average boxiness of less than 0.5%), and a few (e.g., NGC 3489, NGC 4233) because of the impact of dust on the isophote shapes. Among these boxy Fast Rotators, only 17% are clearly barred (8/48): considering the size of that sub-sample, this is not significantly different from the 28% of Fast Rotators which are clearly barred (with this fraction of barred galaxies to be considered as a lower limit). Apart from the mass trend mentioned above, there therefore seems to be no simple link between  $a_4$  of galaxies in the ATLAS<sup>3D</sup> sample and the Slow and Fast Rotator classes.

We also examine whether there is an existing link between the apparent stellar angular momentum measured via  $\lambda_R$  within  $1 R_e$  and the central light excess (or deficit) : these central de-

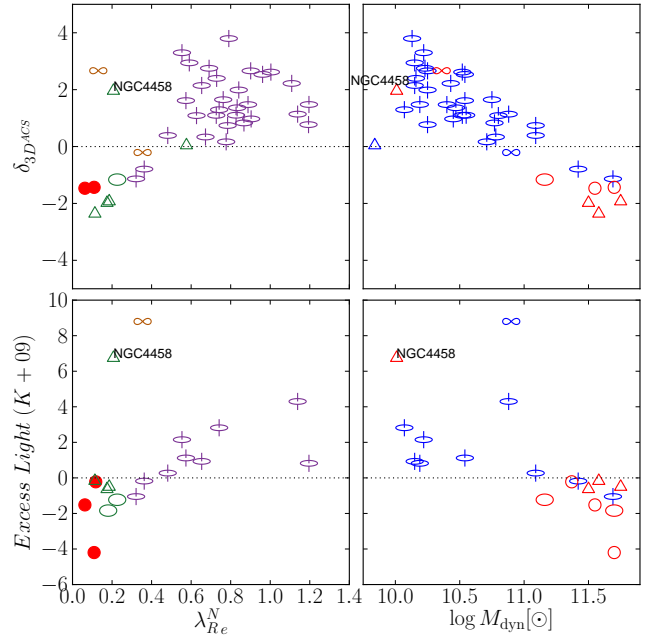


**Figure 14.** The central light deficit as derived by Glass et al. (2011, top panel) and Kormendy et al. (2009, bottom panel), for galaxies in common with the ATLAS<sup>3D</sup> sample, versus  $\lambda_{R_e}^N$  (left panels) and the dynamical mass  $M_{dyn}$  (in log, right panels). Symbols in the right panels are as in Fig. 7, while in the right panels, Slow Rotators are indicated as red symbols, and Fast Rotators as blue symbols. NGC 4458 is emphasised as only galaxy with a KDC (triangle) to have a positive value for the light excess.

partures from simple photometric profiles (Sersic laws) have been interpreted in various contexts but the main processes which have been called upon are dissipational processes (gas filling in the central region and forming stars) to explain the light excesses, and black hole scouring (ejection of stars by binary black holes). In this context, Kormendy et al. (2009) have recently proposed that it represents an important tracer of the past history of the galaxy, and suggested the existence of a dichotomy within the E (elliptical) class of galaxies (see also papers by Khochfar & Burkert 2005; Hopkins et al. 2009a,b,c). In Fig. 14 we present the central excess light value obtained by Kormendy et al. (2009, bottom panel) and Glass et al. (2011, top panel) in terms of the dynamical mass  $\lambda_{R_e}^N$  (left panels) and  $M_{dyn}$  (right panels). We recover the trend already mentioned in Côté et al. (2007), Kormendy et al. (2009) and in Glass et al. (2011), that central light excesses correlate with luminosity (or mass). There is a clear trend for Fast Rotators to have central light excesses, and Slow Rotators to exhibit light deficits. The central light excess is, however, not strongly correlated with the distance to the threshold defining Slow and Fast Rotators, as e.g., Fast Rotators span a wide range of  $\lambda_R/\sqrt{\epsilon}$  values irrespective of the measured central light excess. There is a remarkable exception in Fig. 14 for  $2\sigma$  galaxies which are Slow Rotators but have light excesses: there, morphology and photometry alone fail to reveal the nature of the underlying stellar system, although there may exist associated photometric signatures. NGC 4458 also stands out as a Slow Rotator, with a KDC (*group c*) and having a light excess which seems to correspond to a very central stellar disc (Morelli et al. 2004; Ferrarese et al. 2006). The existing trend between  $\lambda_R$  and total luminosity or mass mentioned in the present paper may be enough to explain the observed trend, e.g., that Slow Rotators exhibit light deficits. However, the small number of objects in Fig. 14

is obviously a major concern in this context, and we should wait for access to larger datasets before we can draw firm conclusions.

## 5 DISCUSSION

The results presented in the previous Sections provide an updated view at ETGs in the nearby Universe, which we first briefly summarise now, before we further discuss the two *families* of Fast and Slow Rotators in turn, and mention how these families can relate to standard physical processes often invoked in the context of galaxy formation and assembly.

The vast majority of ETGs in our sample are Fast Rotators: they dominate in numbers and represent nearly 70% of the stellar mass in ETGs. Fast Rotator are mostly discy galaxies spanning a wide range of apparent ellipticities, the most flattened systems having ellipticities consistent with the ones of spiral galaxies. Slow Rotators represent only 15% of all ETGs in the ATLAS<sup>3D</sup> sample, and only dominate the high mass end of the ETG distribution. We witness three main types of Slow Rotators out of the 36 present in the ATLAS<sup>3D</sup> sample:

- Non-rotating galaxies (4, excluding NGC 6703 which may be a face-on Fast Rotator), which are all more massive than  $10^{11.25} M_{\odot}$ , and appear round, namely NGC 4374, NGC 4486, NGC 4436 and NGC 5846;
- Galaxies which cover a large range of masses (27), often with KDCs (18/27, including NGC 4476 in this set), and are never very flattened with  $\epsilon_e$  smaller than 0.4. This includes 7 galaxies which have KDCs observed as counter-rotating structures;
- Lower-mass flattened  $2\sigma$  galaxies (4), which are interpreted as including two large-scale stellar disc-like counter-rotating components.

The ATLAS<sup>3D</sup> survey probes various galaxy environments, and obviously, the fraction of observed Fast and Slow Rotators would change with samples of galaxies biased towards e.g., higher galaxy densities (Paper VII).

### 5.1 Fast rotators

We can now use our knowledge of the photometric and kinematic structures of Fast Rotators to predict roughly how a given sample of galaxies with particular properties would be distributed if viewed at random inclinations on the sky. A simple prescription could be applied to the family of Fast Rotators, as the vast majority of these exhibits regular stellar velocity maps consistent with apparent disc-like rotation with no significant misalignments between the photometric and kinematic axis (see Paper II for more details on this specific issue). If the galaxies illustrated in Fig. 3, selected to be close to the  $\beta = 0.65 \times \epsilon$  relation for oblate systems, are indeed viewed near edge-on, then Fast Rotators span quite a broad range of intrinsic flattening within  $1 R_e$ . In Fig. 3, the dashed lines emphasise the effect of inclination for galaxies along this relation (see also Appendix B).

We therefore performed Monte-Carlo simulations of a large sample of galaxies following a prescription similar to the one from C+07 (see also Appendix C). We take the distribution for the intrinsic ellipticities  $\epsilon_{intr}$  of the simulated sample as a Gaussian centred at  $\epsilon_0 = 0.7$  with a width  $\sigma_{\epsilon} = 0.2$  for an aperture of  $1 R_e$ . We fixed the  $\beta$  anisotropy distribution also as a Gaussian with a mean of  $m_{\beta} = 0.5$  and a dispersion of  $\sigma_{\beta} = 0.1$  truncated at  $0.8 \times \epsilon_{intr}$  (see C+07). The result of the simulation (50,000 galaxies) is shown

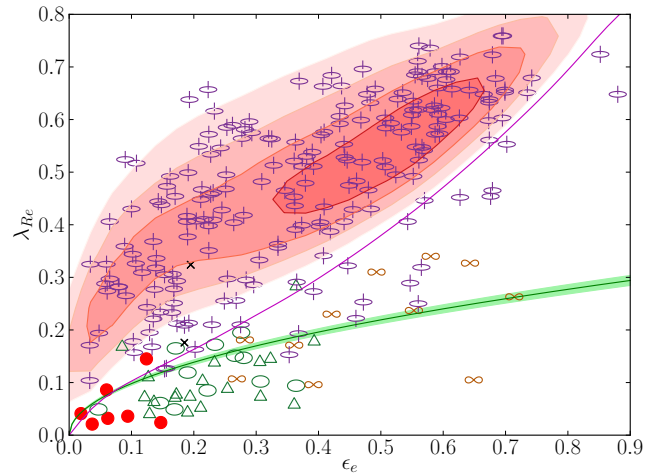


**Figure 15.**  $\lambda_{Re}$  versus apparent ellipticity  $\epsilon_e$  with flags indicating the observed kinematic structure with symbols as in Fig. 7. The coloured contours show the result of Monte Carlo realisations as described in the text. The green line shows the limit between Slow and Fast Rotators.

in Fig. 15, and it is qualitatively consistent with the distribution of Fast Rotators (see also a similar simulation, but for  $R_e/2$  in Appendix B, Fig. B5). This tells us that in this context a reasonable approximation for such galaxies is a set of oblate systems with ellipticities peaking around 0.7, with most of the objects between 0.4 and 0.8. This confirms the visual impression provided in Fig. 3 illustrating the effect of the inclination (dashed lines). This Monte Carlo simulation also tells us that we should expect, from a sample of 224 Fast Rotators, an average of  $\sim 4 \pm 2$  galaxies with  $\lambda_R$  below 0.1, which is consistent with our observed sample.

### 5.2 Slow rotators

Fig. 15 shows, as expected, that slow rotators are clearly inconsistent with the previously simulated dataset. This confirms that the central regions of Slow Rotators are not similar to oblate systems assuming some simple anisotropy-flattening relation as done in the previous Section. Even an ellipticity distribution different from what was assumed in this simulation would not help to cover the region where Slow Rotators are located in a  $\lambda_R$ - $\epsilon$  diagram. Note that galaxies in *group d* have morphologies consistent with oblate systems but have unusually strong tangential anisotropies associated with the presence of two counter-rotating stellar discs. Observed misalignments between the kinematic and photometric axis in Slow Rotators also argue for these to be a different family of galaxies (Paper II) including non-axisymmetric and/or mildly triaxial systems.

As demonstrated Jesseit et al. (2009) and confirmed in Paper V via numerical simulations of mergers, triaxial remnants which are Slow Rotators when viewed edge-on tend to appear as Slow Rotators (stay below the limiting line) for any projection. In the previous Section, we have seen that there is only a low probability for a Fast Rotator to be viewed (due to inclination effects) as a Slow Rotator (something also emphasised by Jesseit et al. 2009), and here we suggest that most galaxies appearing as Slow Rotators would still be Slow Rotators if viewed edge-on. The only cases which are expected to potentially exhibit ambiguous classifications are prolate objects (Naab & Burkert 2003; Jesseit et al. 2005). We have two clear cases in our ATLAS<sup>3D</sup> sample: NGC 4261, and NGC 5485,

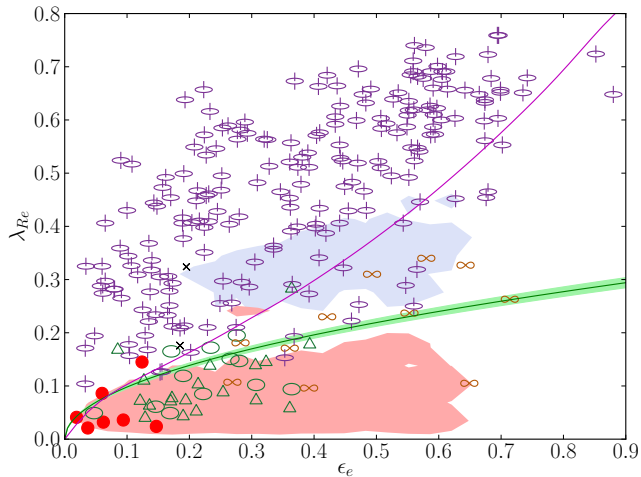


**Figure 16.**  $\lambda_{Re}$  versus apparent ellipticity  $\epsilon_e$  within  $1 R_e$  with symbols as in the bottom panel of Fig. 15. **The blue and red filled coloured areas show the region where 1:1 and 2:1 merger remnants lie from the study of Bois et al. (2011): the red area corresponds to the merger remnants with a retrograde main progenitor (w.r.t. the orbital angular momentum) while the blue area corresponds to a prograde main progenitor.** The green lines show the limit between Slow and Fast Rotators and the magenta line is as in Fig. 7.

the latter being classified as a Fast Rotator here. NGC 5485 is a peculiar galaxy with its photometric major-axis being the symmetry axis for the dust lane and stellar rotation.

### 5.3 Early-type galaxy formation and assembly processes

Various physical processes often invoked for the formation and assembly of galaxies can contribute to or influence the specific angular momentum of the central stellar component of early-type galaxies, and consequently the measured  $\lambda_R$  value, and we briefly review these here in the context of the classification of ETGs into Fast and Slow Rotators.

Dissipative processes followed by star formation should generally help preserving (or rebuilding) stellar rotation in galaxies (see e.g., an early discussion in the context of early-type galaxies in Bender et al. 1992). Accretion of gas from external sources, either via the large-scale filaments (e.g. Sancisi et al. 2008; Dekel et al. 2009; Khochfar & Silk 2009) or extracted by tidal forces from a gas-rich galaxy passing by, thus contribute to an increase of  $\lambda_R$  if the gas is co-rotating with the main existing stellar component, assuming that this additional gas forms stars. This could also be a way for galaxies to rebuild a fast rotating disc-like component. Such a process should preferentially occur in gas-rich environments, e.g., at high redshifts ( $z$  larger than about 2) and/or in low-density regions, disfavouring for instance the inner regions of dense clusters at moderate to low redshifts. An extreme version of such a mechanism is the case of very high gas fractions in disc-like objects, expected to be relevant mostly at high redshift: in such a situation, strong instabilities lead the galaxy to become “clumpy”, with massive gas clouds forming stars and evolving as a  $N$ -body system with low  $N$  (see e.g. Elmegreen et al. 2008, 2009). Evolving in relative isolation, such a system can end up as a disc galaxy (a Fast Rotator, e.g. Bournaud et al. 2008) where the contribution of its spheroidal component varies depending on the exact initial conditions (gas fraction, spatial distribution, angular momentum).

Subsequent evolution due to disc instabilities, spiral density

waves and bars, will tend to heat the stellar component (Sellwood & Binney 2002; Debattista et al. 2006; Sales et al. 2009; Minchev & Famaey 2010), and decrease  $\lambda_R$  accordingly, but the global stellar angular momentum of Fast Rotators should not change dramatically because of such secular evolution processes. Such perturbations could, however, be a trigger for inner gas fuelling then leading to the formation of a central rapidly rotating stellar component (e.g. Wozniak et al. 2003). Similarly, gas stripping from a galaxy, if done in a nearly adiabatic way, should not change  $\lambda_R$  too drastically, even though the system would morphologically and dynamically evolve on a relaxation timescale and this may affect the morphology and dynamics of its central region. This should also concern ram pressure stripping (Gunn & Gott 1972; Quilis, Moore, & Bower 2000; Rasmussen, Ponman, & Mulchaey 2006), or AGN feedback if the major effect remains focused on the gas component.

For a disc-like (spiral) galaxy to become a Slow Rotator, numerical simulations have suggested that it needs to accrete at least half of its stellar mass via mergers (Bournaud et al. 2007; Jesseit et al. 2009; Bois et al. 2010; Bois et al. 2011). As the orbital angular momentum for a (binary) merger event is often the main contributor (Khochfar & Burkert 2006), major mergers can form Fast Rotators (Bois et al. (2011), hereafter Paper VI; and see also Springel & Hernquist (2005)) even from slowly rotating galaxy progenitors (Di Matteo et al. 2009), the outer structure being generally more significantly affected (Coccatto et al. 2009). Numerical studies show anyway that, among binary mergers, only major 1:1 or 2:1 mergers can form Slow Rotators, as it requires enough baryonic angular momentum to be transferred outwards (see Paper VI for details). We illustrate this by indicating where the 1:1 and 2:1 major merger remnants (including gas and star formation) conducted in Paper VI lie in a  $\lambda_R$ - $\epsilon$  diagram in Fig. 16, assuming that the progenitors were spiral galaxies which have  $\lambda_R$  values close to the maximum value observed for our sample of early-type galaxies. There is a clear separation between the merger remnants which are Slow and Fast Rotators: this corresponds to an initially different sign of the spin of the more early-type progenitor (Paper VI) with respect to the orbital angular momentum **as illustrated by the red and blue areas (corresponding to retrograde and prograde spins, respectively) in Fig. 16.** Although such a distinction may be damped if we more broadly sample the input parameters for the progenitors (including their mass ratios) or include more realistic merger trees, the criterion defined here to separate Fast and Slow Rotators seems to properly distinguish two families of galaxies: the merger remnants in Paper VI which are Fast Rotators all have regular velocity fields with small photometric versus kinematic misalignments, while most of the remnants which are Slow Rotators have kpc-size KDCs (see also van den Bosch et al. 2008; Hoffman et al. 2010, Paper VI), and are spread over a wide range of misalignment angle values.

In a similar context, “ $2\sigma$ ” galaxies (10 in our sample, 4 of which are Slow Rotators) clearly stand out in an  $\epsilon$ -Mass diagram within the Slow Rotator class (see Fig. 11), and such systems could be formed when two spiral galaxies with (roughly) opposed spins merge (Crocker et al. 2009). Another scenario relies on the accretion of external and counter-rotating gas in a spiral galaxy (Rubin et al. 1992). Crocker et al. (2009) recently suggested that the sense of rotation of the remnant gas component could indicate which scenario is preferred: associated with the thicker component for the merger scenario, or with the thinner component for the accretion scenario. In the prototype galaxy NGC 4550, the gas rotates with the thicker stellar disc, favouring a merger event. However, other  $2\sigma$  galaxies seem to show various configurations for the gas. We

should also examine more cautiously a broader range of mergers forming such systems, as well as simulate the accretion of counter-rotating gas, before we can go further and constrain the main formation process involved here. In any case, such Slow Rotators very probably require an existing cold, spiral-like progenitor and/or a gas-rich event (merger or accretion). The fact that such Slow Rotators show positive light excess (Fig. 14) contrary to other Slow Rotators is thus naturally explained if they formed and assembled via dissipative processes (accretion or merger), with the excess light being the consequence of a secondary star formation even in the central regions (Mihos & Hernquist 1994; Hopkins et al. 2009c; Kormendy et al. 2009).

To summarise, ways to increase the central specific angular momentum of a galaxy are common, specially at high redshift, and often involve a gaseous dissipational process. Among early-type galaxies, Fast Rotators may therefore be expected to dominate in numbers at low redshifts, as long as the observed sample is not biased towards very dense environments (see Paper VII). The fastest early-type rotators should also be linked to their gas-richer counterpart, namely the spiral galaxies. Indeed, a galaxy like NGC4762 is an excellent illustration of a “dead” spiral with a very high specific (stellar) angular momentum. Other Fast Rotators are the result of a complex history which certainly includes a mix of the processes mentioned in the present Section, and other potentially important ones such as stellar mass loss (see e.g. Martig & Bournaud 2010).

Slow Rotators are the extreme instances of such a mixture of processes, where one of the most violent and disturbing mechanism, namely major or repeated mergers, disrupted their kinematical identity and for which there was little opportunity to transform back into a Fast Rotator: this mostly happens either at the higher end of the mass function (e.g. Khochfar & Burkert 2006; Oser et al. 2010), or, specifically, for low-mass galaxies which are the result of the merging of two counter-rotating (gaseous and/or stellar) components. This picture is consistent with the fact that little or no molecular gas is found in Slow Rotators (Young et al. 2011, Paper IV).

**The detailed structure of nearby ETGs is a consequence of such a (non-exhaustive) list of processes: the exact distribution of ETGs in term of a specific observable, e.g.,  $\lambda_R^N$  (Fig. 9), can then be simply interpreted as the convolution of the impact of each mechanism on that quantity with its relative contribution (this being obviously a naive view considering that each process does not act independently). We should therefore naturally expect a broad and continuous range in the properties of nearby ETGs. Since the relation defined to separate Fast and Slow Rotators is an empirical criterion, i.e. based on observable quantities such as  $\lambda_R$  and  $\epsilon$ , we should also expect a continuous range of properties among Fast Rotators linking them to the Slow Rotators, the final state of an individual galaxy depending on a given (complex) merging/accretion/evolution history. We indeed find galaxies near the dividing line with intermediate properties, and there are a few misclassified systems. Still, the defined criterion for Slow and Fast Rotators operates rather well when the goal is to distinguish galaxies with complex central dynamical structures (e.g., large-scale stellar KDCs), from oblate systems with or without bars. We therefore suggest here that Slow Rotators are the extreme instances of such a mixture of processes where one of the most violent and disturbing mechanism, namely major or repeated mergers, disrupted their kinematical identity and for which there was little opportunity to transform back into a Fast Rotator. This mostly happens either at the higher end of the mass function (e.g.**

**Khochfar & Burkert 2006; Oser et al. 2010), or, specifically, for low-mass galaxies which are the result of the merging of two counter-rotating (gaseous and/or stellar) components. This picture is in fact consistent with the finding that there seems to be little or no molecular gas in Slow Rotators (Young et al. 2011, Paper IV). Most Slow Rotators have a mass above  $10^{10.5}$ , and they clearly dominate the ETG population above  $10^{11.25}$ . If the above-mentioned picture is correct, then the smoothness of the transition between a Fast Rotator dominated to a Slow Rotator dominated population of ETGs should directly depend on the availability of gas and the role of mergers. This is examined in detail in forthcoming papers, e.g., in Khochfar et al. (2011) where semi-analytic modelling techniques suggest that the amount of accreted material and the ability to cool gas and make stars play a prominent role in this context. More specific studies of mergers are presented in Paper VI (numerical simulations of binary mergers) and more specifically in a cosmological context in Naab et al. (2011).**

## 6 CONCLUSIONS

In this paper, we have used photometric and integral-field spectroscopic data to provide the first census of the apparent specific (stellar) angular momentum of a complete sample of 260 early-type galaxies via the  $\lambda_R$  parameter.

We have shown that the apparent kinematic structures can be used to define a refined and optimised criterion to disentangle the so-called Fast and Slow Rotators. This new definition takes into account the fact that at a similar  $\lambda_R$  value, a more flattened galaxy is expected to exhibit a much stronger anisotropy. We are using a simple proxy with Slow Rotators being galaxies which have a specific stellar angular momentum within  $R_e$  as measured by  $\lambda_R$  less than 0.31 (resp. 0.265) times the square root of the ellipticity  $\sqrt{\epsilon}$  measured within an aperture of  $1 R_e$  (resp.  $R_e/2$ ).

Using this relation, we find that  $86 \pm 2\%$  (224/260) of all early-type galaxies in our ATLAS<sup>3D</sup> sample are Fast Rotators. This result, associated with the fact that Fast Rotators in the ATLAS<sup>3D</sup> sample have aligned photometric and kinematic axes within  $5^\circ$  (Paper II), suggest that Fast Rotators are simple oblate systems (with or without bars) which span a range of intrinsic ellipticities between about 0.35 and 0.85. The remaining 14% (36/260) of the ATLAS<sup>3D</sup> sample are Slow Rotators: these are distributed between the well-known massive ( $M > 10^{11} M_\odot$ ) and rather round ( $\epsilon_e < 0.4$ ) galaxies (4 being very massive non-rotators), often exhibiting central Kinematically Decoupled Components, and a set of 4 (or 11% of all Slow Rotators) lower mass objects ( $M_{\text{dyn}} < 10^{10.5} M_\odot$ ) which exhibit two large-scale counter-rotating stellar disc systems (see Paper II for details).

We show that the suggested proxy, namely the  $a_4$  parameter is not efficient at distinguishing Fast Rotators from Slow Rotators. We also conclude that the separation of ETGs into E (elliptical) and S0 (lenticular) classes is misleading. We do observe a trend, as expected, in the sense that most massive Slow Rotators are classified as E’s and most Fast Rotators are classified as S0’s. However, 66% of all E’s in our sample are Fast Rotators, and, apart from a maximum ellipticity of 0.6, these are indistinguishable in our study from the rest of the Fast Rotator population, a result already pointed out in E+07. We provide a quantitative and robust criterion to separate both families, via the  $\lambda_R$  parameter, while we expect only some small overlap around the defined threshold.

Early-type galaxies are the end results of a complex set of for-

18 *Eric Emsellem et al.*

mation and assembly processes, which shaped their morphology and dynamics. From the fastest rotating ETGs, which look like dead and red spirals, down to the slowest Fast Rotators, we observe no obvious discontinuity in their integrated properties. There is, however, a clear increase in the fraction of Slow Rotators above a mass of  $\sim 10^{11.25} M_{\odot}$  (see Sect. 4.7), as well as above a certain local galaxy density (Paper VII). In this context, Slow Rotators represent the extreme instances of such red sequence galaxies for which significant merging has occurred (sometimes with gas-rich systems but then at high redshift), and being at the high end of the mass range of galaxies in the nearby Universe, did not have the opportunity to rebuild a cold stellar component from dissipative processes.

These results argue for a shift in the existing paradigm for early-type galaxies, which are generally separated in disc-like S0 galaxies and spheroidal-like E systems. We find that the vast majority of ETGs in the nearby Universe are Fast Rotators (with 66% of the E's in our sample being Fast Rotators), galaxies consistent with oblate systems with or without bars, while only a small fraction of them (less than 12%), the tail of that distribution encompassing the most massive objects, have central (mildly) triaxial structures reflecting the more standard picture of an ellipsoidal (or spherical) stellar system.

#### ACKNOWLEDGEMENTS

Part of this work has been conducted while visiting the Astronomy Department at University of Texas at Austin under the auspices of a Beatrice Tinsley Scholarship. In this context, EE would like to warmly thank Neal Evans, Gordon Orris and John Kormendy for their hospitality. EE would also like to thank John Kormendy, Laura Ferrarese and Pat Côté for insightful discussions. EE thanks Lisa Glass and Pat Côté for sending an ascii table with the  $\delta_{3D}$  values published in Glass et al. (2011). This work was supported by the Agence Nationale de la Recherche under contract ANR-08-BLAN-0274-01. This work was supported by the rolling grants 'Astrophysics at Oxford' PP/E001114/1 and ST/H002456/1 and visitors grants PPA/V/S/2002/00553, PP/E001564/1 and ST/H504862/1 from the UK Research Councils. RLD acknowledges travel and computer grants from Christ Church, Oxford and support from the Royal Society in the form of a Wolfson Merit Award 502011.K502/jd. RLD also acknowledges the support of the ESO Visitor Programme which funded a 3 month stay in 2010. SK acknowledges support from the the Royal Society Joint Projects Grant JP0869822. TN, SK and MBois acknowledge support from the DFG Cluster of Excellence 'Origin and Structure of the Universe'. MC acknowledges support from a STFC Advanced Fellowship (PP/D005574/1) and a Royal Society University Research Fellowship. MS acknowledges support from a STFC Advanced Fellowship ST/F009186/1. NS and TD acknowledge support from an STFC studentship. RcMd is supported by the Gemini Observatory, which is operated by the Association of Universities for Research in Astronomy, Inc., on behalf of the international Gemini partnership of Argentina, Australia, Brazil, Canada, Chile, the United Kingdom, and the United States of America. The authors acknowledge financial support from ESO.

#### REFERENCES

- Bacon R., Copin Y., Monnet G., Miller B. W., Allington-Smith J. R., Bureau M., Carollo C. M., Davies R. L., Emsellem E., Kuntschner H., Peletier R. F., Verolme E. K., de Zeeuw P. T., 2001, *MNRAS* , 326, 23
- Bell, E. F., et al. 2004, *ApJ* , 608, 752
- Bender, R. 1988, *A&A* , 193, L7
- Bender, R., Burstein, D., & Faber, S. M. 1992, *ApJ* , 399, 462
- Bender, R., Saglia, R. P., & Gerhard, O. E. 1994, *MNRAS* , 269, 785
- Bernardi, M., Shankar, F., Hyde, J. B., Mei, S., Marulli, F., & Sheth, R. K. 2010, *MNRAS* , 404, 2087
- Binney J., 2005, *MNRAS* , 363, 937
- Bois M., Bournaud F., Emsellem, E. et al., 2010, *MNRAS* , 406, 2405
- Bois M., et al., 2011, *MNRAS* , submitted [Paper VI]
- Bournaud, F., Jog, C. J., & Combes, F. 2007, *A&A* , 476, 1179
- Bournaud, F., et al. 2008, *A&A* , 486, 741
- Bournaud, F., et al. 2010, arXiv:1006.4782
- Cappellari, M. 2002, *MNRAS* , 333, 400
- Cappellari M., Copin Y., 2003, *MNRAS* , 342, 345
- Cappellari M., Emsellem E., 2004, *PASP* , 116, 138
- Cappellari M., Emsellem E., Bacon R., Bureau M., Davies R. L., de Zeeuw P. T., Falcón-Barroso J., Krajnović D., Kuntschner H., McDermid R. M., Peletier R. F., Sarzi M., van den Bosch R. C. E., van de Ven G., 2007, *MNRAS* , 379, 418
- Cappellari M., 2008, *MNRAS* , 390, 71
- Cappellari, M., et al. 2010, *Highlights of Astronomy* , 15, 81
- Cappellari M., et al., 2011, *MNRAS* , in press [Paper I], arXiv:1012.1551
- Cappellari M., et al., 2011, *MNRAS* , in press [Paper VII]
- Coccatto, L., et al. 2009, *MNRAS* , 394, 1249
- Côté, P., et al. 2006, *ApJS* , 165, 57
- Côté, P., et al. 2007, *ApJ* , 671, 1456
- Crocker, A. F., Jeong, H., Komugi, S., Combes, F., Bureau, M., Young, L. M., & Yi, S. 2009, *MNRAS* , 393, 1255
- Davies R. L., Efstathiou G., Fall S. M., Illingworth G., Schechter P. L., 1983, *ApJ* , 266, 41
- Debatista, V. P., Mayer, L., Carollo, C. M., Moore, B., Wadsley, J., & Quinn, T. 2006, *ApJ* , 645, 209
- Dekel, A., et al. 2009, *Nature* , 457, 451
- Dekel, A., Sari, R., & Ceverino, D. 2009, *ApJ* , 703, 785
- de Vaucouleurs G., de Vaucouleurs A., Corwin Jr. H. G., Buta R. J., Paturel G., Fouque P., 1991, *Third Reference Catalogue of Bright Galaxies. Volume 1-3, XII, 2069 pp. 7 figs.*. Springer-Verlag Berlin Heidelberg New York
- de Zeeuw P. T., Bureau M., Emsellem E., Bacon R., Carollo C. M., Copin Y., Davies R. L., Kuntschner H., Miller B. W., Monnet G., Peletier R. F., Verolme E. K., 2002, *MNRAS* , 329, 513
- Di Matteo, P., Jog, C. J., Lehnert, M. D., Combes, F., & Semelin, B. 2009, *A&A* , 501, L9
- Elmegreen, B. G., Bournaud, F., & Elmegreen, D. M. 2008, *ApJ* , 688, 67
- Elmegreen, B. G., Elmegreen, D. M., Fernandez, M. X., & Lemoias, J. J. 2009, *ApJ* , 692, 12
- Emsellem, E., Monnet, G., & Bacon, R. 1994, *A&A* , 285, 723
- Emsellem E., Cappellari M., Peletier R. F., McDermid R. M., Bacon R., Bureau M., Copin Y., Davies R. L., Krajnović D., Kuntschner H., Miller B. W., de Zeeuw P. T., 2004, *MNRAS* , 352, 721
- Emsellem, E., et al. 2007, *MNRAS* , 379, 401
- Ferrarese, L., et al. 2006, *ApJS* , 164, 334
- Fukugita, M., et al. 2007, *AJ* , 134, 579

*The ATLAS<sup>3D</sup> project – III. A census of the stellar angular momentum in ETGs* 19

- Geha, M., Guhathakurta, P., & van der Marel, R. P. 2005, *AJ*, 129, 2617
- Gerhard, O. E., Jeske, G., Saglia, R. P., & Bender, R. 1999, *Galaxy Interactions at Low and High Redshift*, 186, 189
- Glass, L., et al. 2011, *ApJ*, 726, 31
- Graham, A. W. 2004, *ApJ*, 613, L33
- Graham, A. W., & Guzmán, R. 2003, *AJ*, 125, 2936
- Gunn J. E., Gott J. R., III, 1972, *ApJ*, 176, 1
- Hoffman, L., Cox, T. J., Dutta, S., & Hernquist, L. 2010, *ApJ*, 723, 818
- Hopkins, P. F., Cox, T. J., Dutta, S. N., Hernquist, L., Kormendy, J., & Lauer, T. R. 2009, *ApJS*, 181, 135
- Hopkins, P. F., Hernquist, L., Cox, T. J., Keres, D., & Wuyts, S. 2009, *ApJ*, 691, 1424
- Hopkins, P. F., Lauer, T. R., Cox, T. J., Hernquist, L., & Kormendy, J. 2009, *ApJS*, 181, 486
- Hubble E. P., 1936, *Realm of the Nebulae*, Yale University Press
- Jarrett, T. H., Chester, T., Cutri, R., Schneider, S., Skrutskie, M., & Huchra, J. P. 2000, *AJ*, 119, 2498
- Jesseit, R., Naab, T., & Burkert, A. 2005, *MNRAS*, 360, 1185
- Jesseit, R., Naab, T., Peletier, R. F., & Burkert, A. 2007, *MNRAS*, 376, 997
- Jesseit, R., Cappellari, M., Naab, T., Emsellem, E., & Burkert, A., 2009, *MNRAS*, 397, 1202
- Khochfar S., Burkert A., 2003, *ApJ*, 597, L117
- Khochfar S., Burkert A., 2005, *MNRAS*, 359, 1379
- Khochfar S., Burkert A., 2006, *A&A*, 445, 403
- Khochfar S., Silk J., 2009, *ApJ*, 700, L21
- Khochfar M., et al., 2011, *MNRAS*, submitted [Paper VIII]
- Kormendy J., Bender R., 1996, *ApJ*, 464, L119+
- Kormendy, J., Fisher, D. B., Cornell, M. E., & Bender, R. 2009, *ApJS*, 182, 216
- Krajnović D., Cappellari M., de Zeeuw P. T., Copin Y., 2006, *MNRAS*, 366, 787
- Krajnović, D., et al. 2008, *MNRAS*, 390, 93
- Krajnović D., et al., 2011, *MNRAS*, submitted [Paper II]
- Kriek, M., van der Wel, A., van Dokkum, P. G., Franx, M., & Illingworth, G. D. 2008, *ApJ*, 682, 896
- Kuntschner H., Emsellem E., Bacon R., Bureau M., Cappellari M., Davies R. L., de Zeeuw P. T., Falcón-Barroso J., Krajnović D., McDermid R. M., Peletier R. F., Sarzi M., 2006, *MNRAS*, 369, 497
- Kuntschner, H., et al. 2010, *MNRAS*, 1215
- Li, J. G., & Seaquist, E. R. 1994, *AJ*, 107, 1953
- Martig, M., & Bournaud, F. 2010, *ApJ*, 714, L275
- McIntosh, D. H., et al. 2005, *ApJ*, 632, 191
- Mihos, J. C., & Hernquist, L. 1994, *ApJ*, 437, L47
- Minchev, I., & Famaey, B. 2010, *ApJ*, 722, 112
- Morelli, L., et al. 2004, *MNRAS*, 354, 753
- Naab, T., Burkert, A., & Hernquist, L. 1999, *ApJ*, 523, L133
- Naab, T., & Burkert, A. 2001, *ApJ*, 555, L91
- Naab, T., & Burkert, A. 2003, *ApJ*, 597, 893
- Naab, T., Johansson, P. H., Ostriker, J. P., & Efstathiou, G. 2007, *ApJ*, 658, 710
- Naab, T., Johansson, P. H., & Ostriker, J. P. 2009, *ApJ*, 699, L178
- Naab T., et al., 2011, *MNRAS*, in preparation
- Oser, L., Ostriker, J. P., Naab, T., Johansson, P. H., & Burkert, A. 2010, *ApJ*, 725, 2312
- Paturel, G., Petit, C., Prugniel, P., Theureau, G., Rousseau, J., Brouty, M., Dubois, P., & Cambrésy, L. 2003, *A&A*, 412, 45
- Quilis V., Moore B., Bower R., 2000, *Sci*, 288, 1617
- Rasmussen J., Ponman T. J., Mulchaey J. S., 2006, *MNRAS*, 370, 453
- Rix, H.-W., & White, S. D. M. 1990, *ApJ*, 362, 52
- Rix H.-W., Franx M., Fisher D., Illingworth G., 1992, *ApJ*, 400, L5
- Rix, H.-W., Carollo, C. M., & Freeman, K. 1999, *ApJ*, 513, L25
- Rubin, V. C., Graham, J. A., & Kenney, J. D. P. 1992, *ApJ*, 394, L9
- Sales, L. V., et al. 2009, *MNRAS*, 400, L61
- Sánchez-Blázquez, P., et al. 2006, *MNRAS*, 371, 703
- Sancisi, R., Fraternali, F., Oosterloo, T., & van der Hulst, T. 2008, *A&A Rev.*, 15, 189
- Sarzi M., Falcón-Barroso J., Davies R. L., Bacon R., Bureau M., Cappellari M., de Zeeuw P. T., Emsellem E., Fathi K., Krajnović D., Kuntschner H., McDermid R. M., Peletier R. F., 2006, *MNRAS*, 366, 1151
- Scorza, C., & van den Bosch, F. C. 1998, *MNRAS*, 300, 469
- Scott N., et al., 2009, *MNRAS*, 398, 1835
- Sellwood, J. A., & Binney, J. J. 2002, *MNRAS*, 336, 785
- Springel, V., & Hernquist, L. 2005, *ApJ*, 622, L9
- van den Bosch, R. C. E., van de Ven, G., Verolme, E. K., Cappellari, M., & de Zeeuw, P. T. 2008, *MNRAS*, 385, 647
- Wozniak, H., Combes, F., Emsellem, E., & Friedli, D. 2003, *A&A*, 409, 469
- Young L., et al., 2011, *MNRAS*, in press [Paper IV]

#### APPENDIX A: STELLAR VELOCITY AND DISPERSION MAPS OF SLOW ROTATORS IN THE ATLAS<sup>3D</sup> SAMPLE

We provide here two figures (Figs. A1 and A1) illustrating the stellar velocity and dispersion maps for the 36 slow rotators of our ATLAS<sup>3D</sup> sample. Galaxies are sorted by (increasing) mass from left to right, top to bottom.

**Fig. A1 emphasises the non-regularity of the velocity fields of Slow Rotators, as well as the presence of large-scale (kpc-size) KDCs. It also illustrates that the galaxies with zero apparent rotation (NGC 4374, NGC 4486 and NGC 5846) are among the most massive Slow Rotators. The dispersion maps provided in Fig. A2 illustrate e.g., how the stellar velocity dispersion peaks along the major-axis away from the centre for the Slow Rotators which were labelled "double  $\sigma$ " in Krajnović et al. (2011): these systems (e.g., NGC 4550 and NGC 4528) are on the low-mass end of our sample.**

#### APPENDIX B: DYNAMICAL MODELS, $V/\sigma$ AND $\lambda_R$

In E+07 (see their Appendix B), it has been shown that a tight relation exists between  $\lambda_R$  and  $V/\sigma$  for simple two-integral Jeans models, namely:

$$\lambda_R = \frac{\langle RV \rangle}{\langle R\sqrt{V^2 + \sigma^2} \rangle} \approx \frac{\kappa (V/\sigma)}{\sqrt{1 + \kappa^2 (V/\sigma)^2}}. \quad (\text{B1})$$

The value of  $\kappa$  was estimated both from observations and models to be  $\sim 1.1$ .

Here we wish to extend this work both for our complete ATLAS<sup>3D</sup> sample and additional models. We have now derived a series of dynamical models for ellipsoidal or spheroidal systems with various intrinsic flattening (with ellipticities from 0 to 0.9), luminosity (or mass) profiles (Sersic profiles with  $n = 2$

20 *Eric Emsellem et al.*

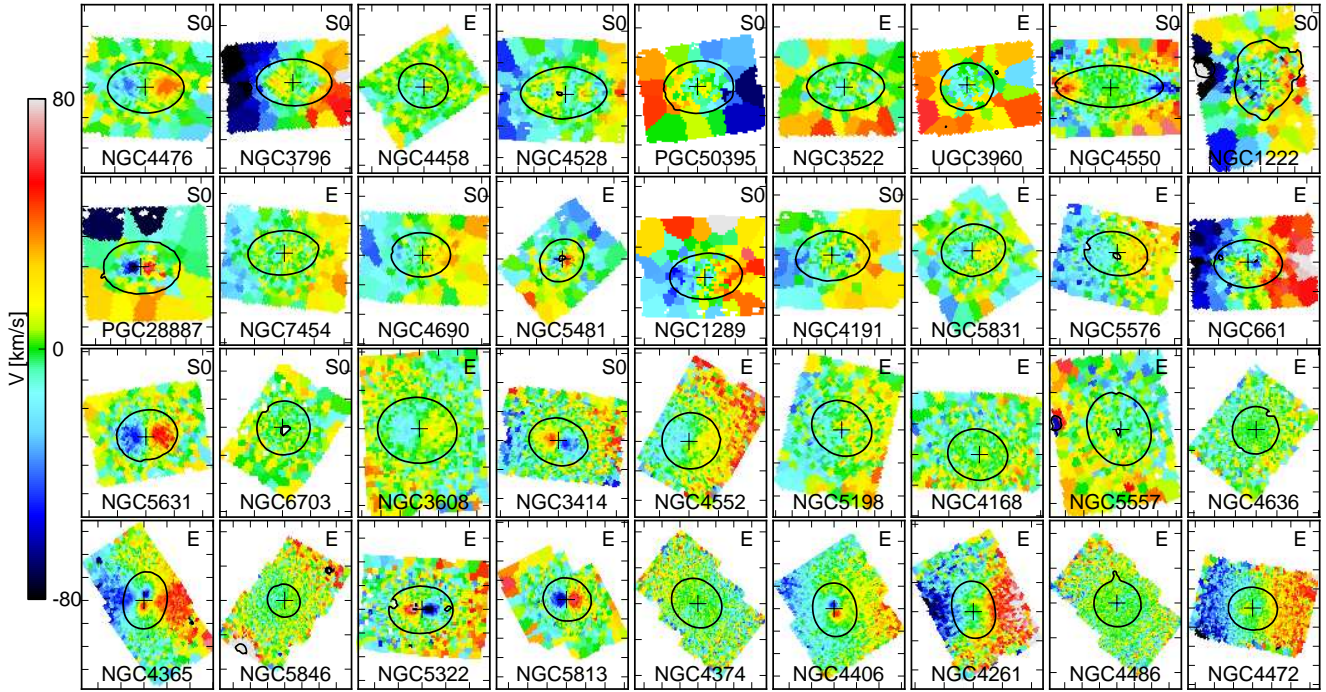


**Figure A1.** Stellar velocity fields for the 36 early-type slow rotators in the ATLAS<sup>3D</sup> sample. We used the kinematic axis to align all galaxies horizontally. Colour cuts have been adapted to each individual map. The solid black contour correspond to a representative isophote and the centre of the galaxy is indicated by a cross. From top to bottom, left to right, the order follows the (increasing) dynamical mass values. The names of the galaxies and their Hubble types (E or S0) are also indicated. The colour cuts have been set up to  $\pm 80$  [km.s<sup>-1</sup>] for all maps.

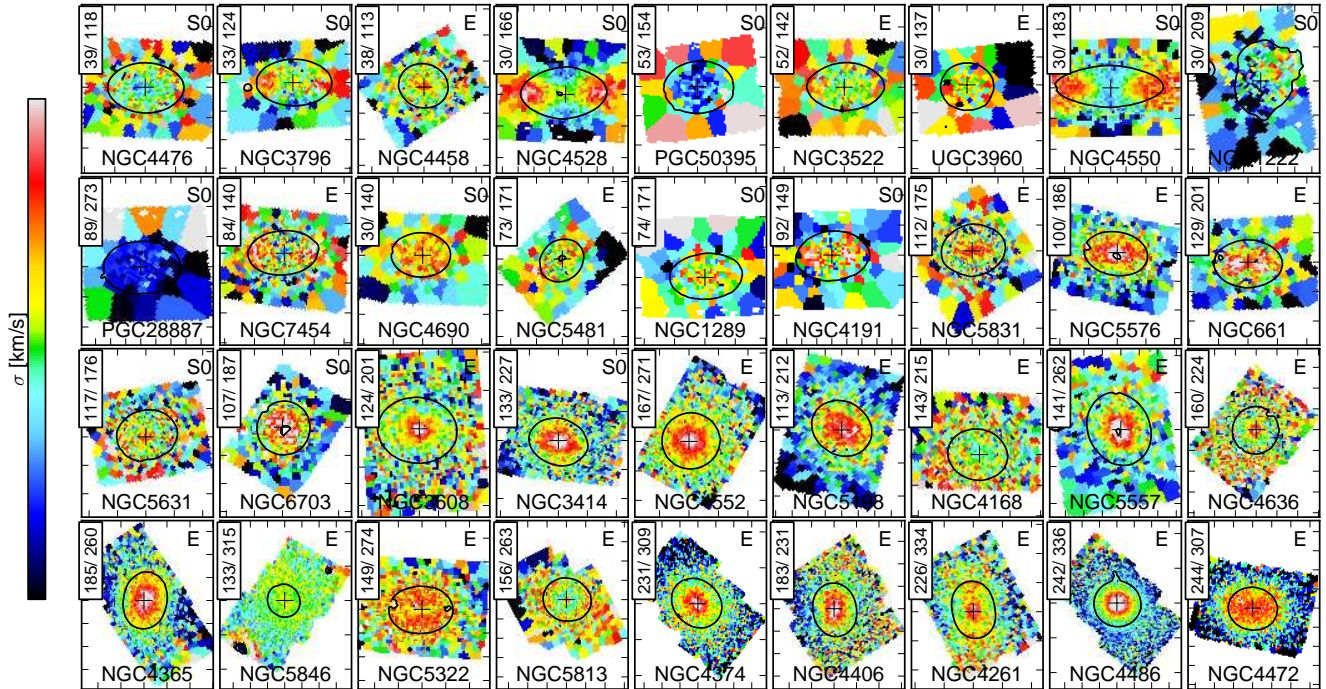


**Figure A2.** Stellar velocity dispersion fields for the 36 early-type slow rotators in the ATLAS<sup>3D</sup> sample. See Fig. A1 for details. The specific colour cuts adapted to each dispersion map are specified in each inset (in km.s<sup>-1</sup>).

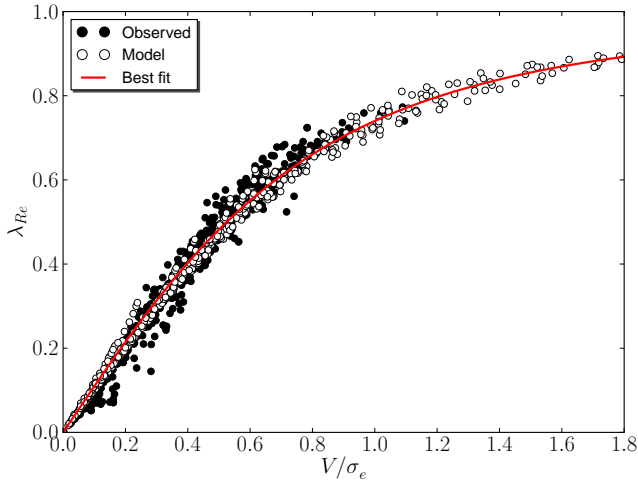
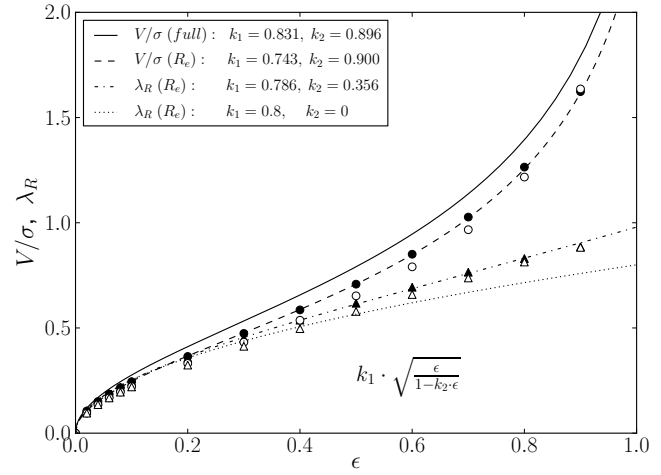


**Figure B1.**  $\lambda_R$  versus  $V/\sigma$  from the relation given in Eq. B1. Results from the dynamical models are shown as open circles, and measurements resulting from the ATLAS<sup>3D</sup> observations as black circles. The solid red line is the best fit relation following Eq. B1 with  $\kappa = 1.1$ . Note that the observations exhibit a slightly steeper slope.

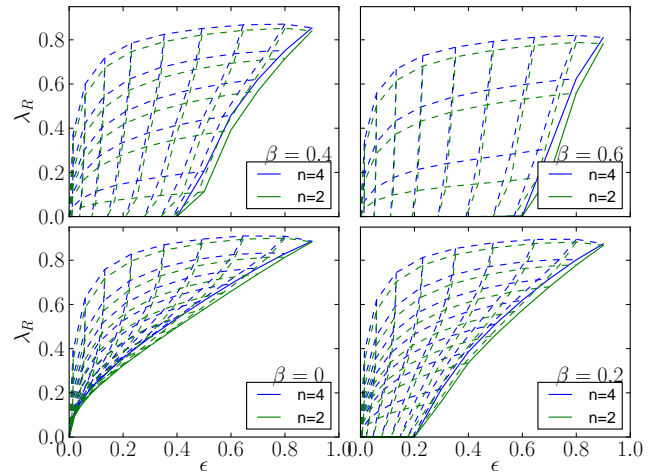
or 4), and anisotropy parameters ( $\beta$  from 0 to 0.6). The dynamical models have an axisymmetric mass distribution described by the MGE parametrization (Emsellem et al. 1994), which was derived by fitting a one-dimensional Sersic profile with the MGE routines of Cappellari (2002). The models assume a spatially-constant, cylindrically-aligned and oblate ( $\sigma_\phi = \sigma_R$ ) velocity ellipsoid (where  $\sigma_\phi$  and  $\sigma_R$  are the azimuthal and radial velocity dispersion, respectively) characterized by the anisotropy parameter  $\beta = 1 - (\sigma_z/\sigma_R)^2$ . Under these assumptions the unique prediction for the two-dimensional  $V$  and  $\sigma$  field for the models was computed by solving the anisotropic Jeans equations with the routines of Cappellari (2008). The two-dimensional kinematics of the models was projected at different inclinations and was integrated within elliptical apertures of effective radii  $R_e$  or  $R_e/2$ , in the same way as for the observed systems.

We first confirm that  $\kappa = 1.1$  for Eq. B1 provides a good fit for both the models and our complete ATLAS<sup>3D</sup> sample (see Fig. B1), although the slope is slightly steeper for the observed galaxies than for the models, and the optimal value does in fact vary significantly depending on inclination and anisotropy. We present the predictions of these models for  $\lambda_R$  versus  $\epsilon$  for anisotropy  $\beta$  values from 0 to 0.6 in Fig. B3, and for apertures of  $1 R_e$  and  $R_e/2$ , in Fig. B4. Assuming a relation of the form given in Eq. B1 hold between  $V/\sigma$  and  $\lambda_R$ , we can translate any relation such as  $(V/\sigma)(x_1) = C \cdot (V/\sigma)(x_2)$  by  $f_{\lambda_R}(x_1) = C \cdot f_{\lambda_R}(x_2)$  where  $f_{\lambda_R} = \lambda_R/\sqrt{1 - \lambda_R^2}$ . We find that generally  $(V/\sigma)_e \sim 1.1 (V/\sigma)_{e/2}$ , and accordingly that  $f_{\lambda_R}(R_e) \sim 1.15 \cdot f_{\lambda_R}(R_e/2)$ : the constant of proportionality slightly changes from 1.1 to 1.15 here mainly because  $\kappa$  in Eq. B1 is not exactly constant as we go to smaller apertures.

We then provide the best fit relations for  $\lambda_R$  and  $V/\sigma$  as functions of ellipticity  $\epsilon$  for isotropic systems, as given by  $k_1 \sqrt{\frac{\epsilon}{1 - k_2 \epsilon}}$ . The theoretical values for  $k_1$  and  $k_2$  are 0.831 and 0.896, using the entire dynamical system and assuming  $\alpha = 0.15$  (see Binney 2005). This corresponds to values of  $k_1 \sim 0.90$  and  $k_2 \sim 0.08$  for  $\lambda_R$ . This means that  $\lambda_R$  is nearly proportional to  $\sqrt{\epsilon}$  for isotropic systems (with  $\alpha = 0.15$ ), leading to a reasonable approximation for low values of the ellipticity with  $\lambda_R \sim 0.91 \times \sqrt{\epsilon}$ , and a best



**Figure B2.**  $\lambda_R$  (triangles) and  $V/\sigma$  (circles) as functions of the ellipticity  $\epsilon$  for isotropic systems: the expected theoretical formula is shown as a solid line (with  $\alpha = 0.15$ , see Binney 2005, for details and notations), while the dashed and dashed-dotted lines provide the best fits to the edge-on values for  $V/\sigma$  and  $\lambda_R$  derived within  $1 R_e$ , respectively. Filled and open symbols are for mass profiles with Sersic index  $n = 4$  and  $n = 2$ , respectively. The dotted line shows the approximation using a simple law where  $\lambda_R \propto \sqrt{\epsilon}$ .

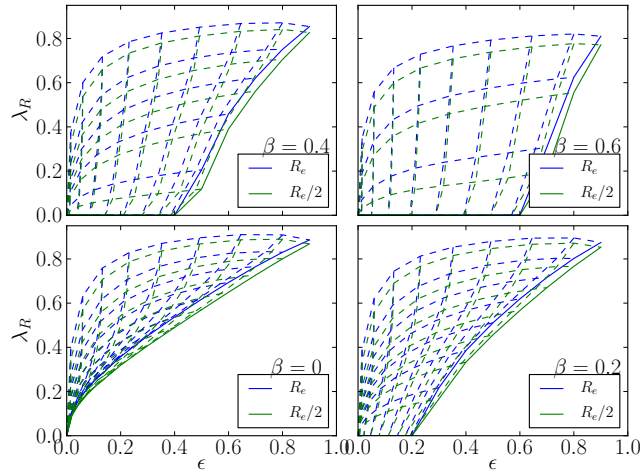


**Figure B3.**  $\lambda_R$  versus the ellipticity  $\epsilon$  for different values of the anisotropy parameter  $\beta$  and two Sersic profiles ( $n = 2$  and  $n = 4$ ).

fit approximation over a range  $[0 - 0.9]$  of ellipticities given by  $0.93 \sqrt{\epsilon}$ . As shown in C+07, the expected values using an effective aperture of  $R_e/2$  are slightly smaller but would be close to the theoretical values obtained with  $\alpha \sim 0.2$ . The best fit relation for edge-on values within  $1 R_e$  gives  $k_1 = 0.743$  and  $k_2 = 0.900$  for  $V/\sigma$ . There is a slight dependency of these parameters when the mass profile is changed (Sersic index  $n = 4$  and  $n = 2$ ), as expected.

The corresponding (edge-on) best fit relation for  $\lambda_R$  provides  $k_1 = 0.786$  and  $k_2 = 0.355$  for apertures of  $1 R_e$ , and  $k_1 = 0.69$  and  $k_2 = 0.50$  for  $R_e/2$ . Restricting ourselves to the lower range of ellipticities (below 0.35), we have  $\lambda_R \sim 0.8 \times \sqrt{\epsilon}$  and  $\lambda_R \sim 0.71 \times \sqrt{\epsilon}$  for apertures of  $1 R_e$  and  $R_e/2$ , respectively.

It is worth mentioning the effect on inclination for both  $V/\sigma$  and  $\lambda_R$  values. As shown by Binney (2005), for an inclination  $i$ ,

22 *Eric Emsellem et al.*

**Figure B4.**  $\lambda_R$  versus the ellipticity  $\epsilon$  for apertures of  $1 R_e$  and  $R_e/2$ .

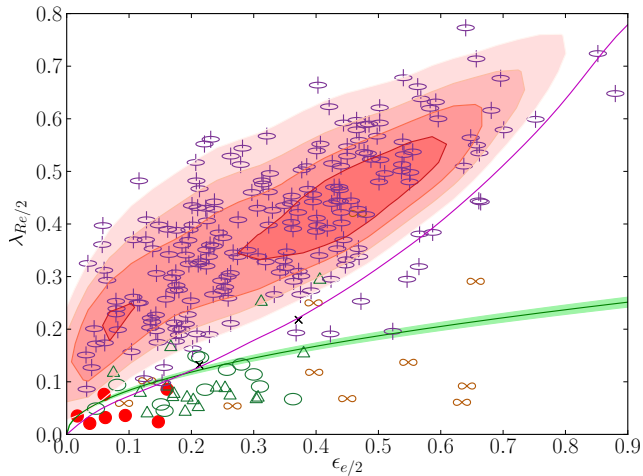


**Figure B5.**  $\lambda_{R_e/2}$  versus apparent ellipticity  $\epsilon_{e/2}$  with flags indicating the observed kinematic structure with symbols as in Fig. 7. The coloured contours show the result of a Monte Carlo realisation as described in the text. The green line shows the limit between Slow and Fast Rotators.

we have ( $i = 90^\circ$  being edge-on):

$$(V/\sigma)(i) = C(i) \cdot (V/\sigma)_{\text{edge-on}}$$

with  $C(i) = \sin i / \sqrt{1 - \beta \cos^2 i}$  where we assumed an axisymmetric system for which the intersection between the velocity ellipsoid and a plane perpendicular to the axis of symmetry is a circle everywhere. Assuming the relation B1 holds, this translates into:

$$\lambda_R(i) = C(i) \cdot \frac{\lambda_{R_{\text{edge-on}}}}{\sqrt{1 + (C^2(i) - 1) \cdot \lambda_{R_{\text{edge-on}}}^2}}$$

We finally include in Fig. B5 a Monte Carlo simulation as in Fig. 15 (see Sect. 5.1) but here for a smaller aperture of  $R_e/2$  for comparison. We use a distribution for the intrinsic ellipticities  $\epsilon_{\text{intr}}$  of the simulated sample with two Gaussians: one centred at  $\epsilon_0 = 0.7$  with a width  $\sigma_\epsilon = 0.2$  as for the simulation at  $1 R_e$ , and we add one component centred at  $\epsilon_0 = 0.6$  representing 30% of the one at 0.7. This second Gaussian is required to account for the fact that for an aperture of  $R_e/2$  the intrinsic ellipticity distribution is offset to values slightly smaller than for an aperture size of  $R_e$ ,

the larger one better probing the outer more flattened component of (most) Fast Rotators. We again fix the anisotropy distribution also as a Gaussian with a mean of  $m_\beta = 0.5$  and a dispersion of  $\sigma_\beta = 0.1$ , truncated at  $0.8\epsilon_{\text{intr}}$ .

*The ATLAS<sup>3D</sup> project – III. A census of the stellar angular momentum in ETGs* 23

Table B1. Ellipticities,  $\lambda_R$  and  $V/\sigma$  tabulated values for the ATLAS<sup>3D</sup> sample or 260 early-type galaxies

| Name    | $R_{max}$ | $\epsilon_e$ | $\epsilon_{e/2}$ | $Band(\epsilon)$ | $V/\sigma_e$ | $V/\sigma_{e/2}$ | $\lambda_{Re}$ | $\lambda_{Re/2}$ | F/S ( $R_e$ ) | F/S ( $R_e/2$ ) |
|---------|-----------|--------------|------------------|------------------|--------------|------------------|----------------|------------------|---------------|-----------------|
| (1)     | (2)       | (3)          | (4)              | (5)              | (6)          | (7)              | (8)            | (9)              | (10)          | (11)            |
| IC0560  | 1.57      | 0.587        | 0.479            | G                | 0.770        | 0.607            | 0.691          | 0.589            | F             | F               |
| IC0598  | 1.94      | 0.579        | 0.502            | G                | 0.896        | 0.629            | 0.736          | 0.592            | F             | F               |
| IC0676  | 0.88      | 0.524        | 0.664            | G                | 0.508        | 0.436            | 0.495          | 0.442            | F             | F               |
| IC0719  | 1.60      | 0.714        | 0.642            | R                | 0.279        | 0.117            | 0.263          | 0.092            | F             | S               |
| IC0782  | 0.92      | 0.404        | 0.263            | G                | 0.677        | 0.608            | 0.571          | 0.529            | F             | F               |
| IC1024  | 1.81      | 0.679        | 0.752            | G                | 0.916        | 0.647            | 0.723          | 0.599            | F             | F               |
| IC3631  | 1.49      | 0.560        | 0.523            | G                | 0.218        | 0.173            | 0.250          | 0.196            | F             | F               |
| NGC0448 | 1.78      | 0.643        | 0.656            | G                | 0.380        | 0.377            | 0.327          | 0.291            | F             | F               |
| NGC0474 | 0.61      | 0.192        | 0.191            | G                | 0.229        | 0.227            | 0.213          | 0.210            | F             | F               |
| NGC0502 | 1.73      | 0.146        | 0.047            | G                | 0.213        | 0.168            | 0.234          | 0.172            | F             | F               |
| NGC0509 | 0.84      | 0.679        | 0.661            | G                | 0.451        | 0.430            | 0.465          | 0.444            | F             | F               |
| NGC0516 | 1.40      | 0.699        | 0.701            | G                | 0.786        | 0.625            | 0.656          | 0.579            | F             | F               |
| NGC0524 | 0.71      | 0.034        | 0.034            | G                | 0.344        | 0.344            | 0.325          | 0.325            | F             | F               |
| NGC0525 | 1.78      | 0.280        | 0.173            | G                | 0.404        | 0.285            | 0.418          | 0.274            | F             | F               |
| NGC0661 | 1.50      | 0.306        | 0.307            | G                | 0.134        | 0.094            | 0.139          | 0.070            | S             | S               |
| NGC0680 | 1.39      | 0.189        | 0.185            | G                | 0.413        | 0.361            | 0.406          | 0.360            | F             | F               |
| NGC0770 | 2.36      | 0.276        | 0.300            | G                | 0.185        | 0.117            | 0.195          | 0.114            | F             | S               |
| NGC0821 | 0.60      | 0.392        | 0.392            | G                | 0.288        | 0.288            | 0.273          | 0.273            | F             | F               |
| NGC0936 | 0.99      | 0.223        | 0.223            | C                | 0.656        | 0.421            | 0.644          | 0.402            | F             | F               |
| NGC1023 | 0.55      | 0.363        | 0.363            | G                | 0.372        | 0.372            | 0.391          | 0.391            | F             | F               |
| NGC1121 | 2.77      | 0.559        | 0.450            | G                | 0.828        | 0.587            | 0.711          | 0.547            | F             | F               |
| NGC1222 | 1.54      | 0.280        | 0.280            | C                | 0.157        | 0.134            | 0.146          | 0.127            | S             | S               |
| NGC1248 | 1.30      | 0.227        | 0.138            | G                | 0.522        | 0.337            | 0.534          | 0.353            | F             | F               |
| NGC1266 | 1.02      | 0.193        | 0.207            | G                | 0.775        | 0.589            | 0.638          | 0.517            | F             | F               |
| NGC1289 | 1.13      | 0.393        | 0.380            | G                | 0.172        | 0.154            | 0.178          | 0.154            | S             | S               |
| NGC1665 | 0.83      | 0.491        | 0.440            | G                | 0.669        | 0.478            | 0.658          | 0.510            | F             | F               |
| NGC2481 | 1.92      | 0.684        | 0.467            | G                | 0.686        | 0.399            | 0.678          | 0.428            | F             | F               |
| NGC2549 | 1.18      | 0.587        | 0.488            | G                | 0.623        | 0.563            | 0.572          | 0.523            | F             | F               |
| NGC2577 | 1.42      | 0.471        | 0.421            | G                | 0.874        | 0.733            | 0.696          | 0.623            | F             | F               |
| NGC2592 | 1.65      | 0.208        | 0.210            | G                | 0.529        | 0.422            | 0.549          | 0.431            | F             | F               |
| NGC2594 | 3.24      | 0.403        | 0.434            | G                | 0.455        | 0.450            | 0.404          | 0.444            | F             | F               |
| NGC2679 | 0.93      | 0.368        | 0.368            | G                | 0.185        | 0.185            | 0.193          | 0.193            | F             | F               |
| NGC2685 | 1.04      | 0.612        | 0.592            | G                | 0.840        | 0.734            | 0.691          | 0.632            | F             | F               |
| NGC2695 | 1.24      | 0.293        | 0.225            | G                | 0.582        | 0.422            | 0.575          | 0.406            | F             | F               |
| NGC2698 | 1.60      | 0.516        | 0.267            | S                | 0.569        | 0.331            | 0.593          | 0.345            | F             | F               |
| NGC2699 | 1.73      | 0.143        | 0.202            | G                | 0.450        | 0.393            | 0.444          | 0.398            | F             | F               |
| NGC2764 | 1.68      | 0.614        | 0.662            | G                | 0.783        | 0.568            | 0.658          | 0.535            | F             | F               |
| NGC2768 | 0.43      | 0.472        | 0.472            | G                | 0.236        | 0.236            | 0.253          | 0.253            | F             | F               |
| NGC2778 | 1.28      | 0.224        | 0.201            | G                | 0.574        | 0.419            | 0.572          | 0.435            | F             | F               |
| NGC2824 | 2.91      | 0.162        | 0.107            | G                | 0.533        | 0.407            | 0.492          | 0.370            | F             | F               |
| NGC2852 | 3.03      | 0.135        | 0.044            | G                | 0.320        | 0.186            | 0.368          | 0.201            | F             | F               |
| NGC2859 | 0.79      | 0.089        | 0.057            | G                | 0.410        | 0.408            | 0.359          | 0.361            | F             | F               |
| NGC2880 | 0.98      | 0.282        | 0.208            | G                | 0.627        | 0.508            | 0.581          | 0.482            | F             | F               |
| NGC2950 | 1.33      | 0.362        | 0.237            | G                | 0.488        | 0.472            | 0.436          | 0.428            | F             | F               |
| NGC2962 | 0.80      | 0.484        | 0.319            | G                | 0.376        | 0.298            | 0.430          | 0.328            | F             | F               |
| NGC2974 | 0.66      | 0.407        | 0.403            | R                | 0.813        | 0.811            | 0.663          | 0.664            | F             | F               |
| NGC3032 | 1.54      | 0.102        | 0.176            | G                | 0.267        | 0.173            | 0.344          | 0.201            | F             | F               |
| NGC3073 | 1.53      | 0.124        | 0.161            | G                | 0.136        | 0.092            | 0.145          | 0.086            | F             | S               |
| NGC3098 | 1.53      | 0.552        | 0.440            | S                | 0.744        | 0.446            | 0.635          | 0.422            | F             | F               |
| NGC3156 | 1.16      | 0.478        | 0.469            | G                | 0.771        | 0.611            | 0.648          | 0.559            | F             | F               |

Table B1 (cont'd)

| Name    | $R_{max}$ | $\epsilon_e$ | $\epsilon_{e/2}$ | $Band(\epsilon)$ | $V/\sigma_e$ | $V/\sigma_{e/2}$ | $\lambda_{Re}$ | $\lambda_{Re/2}$ | F/S ( $R_e$ ) | F/S ( $R_e/2$ ) |
|---------|-----------|--------------|------------------|------------------|--------------|------------------|----------------|------------------|---------------|-----------------|
| (1)     | (2)       | (3)          | (4)              | (5)              | (6)          | (7)              | (8)            | (9)              | (10)          | (11)            |
| NGC3182 | 0.97      | 0.166        | 0.195            | G                | 0.372        | 0.405            | 0.306          | 0.369            | F             | F               |
| NGC3193 | 0.76      | 0.129        | 0.143            | G                | 0.208        | 0.208            | 0.195          | 0.197            | F             | F               |
| NGC3226 | 0.67      | 0.168        | 0.159            | G                | 0.273        | 0.275            | 0.251          | 0.257            | F             | F               |
| NGC3230 | 1.08      | 0.550        | 0.360            | G                | 0.617        | 0.393            | 0.609          | 0.403            | F             | F               |
| NGC3245 | 0.79      | 0.442        | 0.444            | G                | 0.624        | 0.579            | 0.626          | 0.592            | F             | F               |
| NGC3248 | 1.29      | 0.374        | 0.290            | G                | 0.514        | 0.380            | 0.511          | 0.350            | F             | F               |
| NGC3301 | 1.02      | 0.507        | 0.324            | G                | 0.676        | 0.550            | 0.603          | 0.461            | F             | F               |
| NGC3377 | 0.57      | 0.503        | 0.503            | G                | 0.564        | 0.564            | 0.522          | 0.522            | F             | F               |
| NGC3379 | 0.70      | 0.104        | 0.104            | G                | 0.152        | 0.152            | 0.157          | 0.157            | F             | F               |
| NGC3384 | 0.63      | 0.065        | 0.058            | G                | 0.456        | 0.449            | 0.406          | 0.397            | F             | F               |
| NGC3400 | 1.20      | 0.437        | 0.437            | C                | 0.763        | 0.435            | 0.660          | 0.423            | F             | F               |
| NGC3412 | 0.67      | 0.441        | 0.441            | C                | 0.346        | 0.341            | 0.370          | 0.364            | F             | F               |
| NGC3414 | 0.83      | 0.194        | 0.193            | G                | 0.106        | 0.107            | 0.073          | 0.070            | S             | S               |
| NGC3457 | 1.51      | 0.033        | 0.032            | S                | 0.110        | 0.092            | 0.104          | 0.086            | F             | F               |
| NGC3458 | 1.79      | 0.231        | 0.114            | G                | 0.439        | 0.245            | 0.461          | 0.250            | F             | F               |
| NGC3489 | 0.89      | 0.262        | 0.221            | G                | 0.687        | 0.621            | 0.589          | 0.552            | F             | F               |
| NGC3499 | 2.31      | 0.139        | 0.143            | G                | 0.323        | 0.236            | 0.318          | 0.227            | F             | F               |
| NGC3522 | 2.00      | 0.361        | 0.262            | S                | 0.080        | 0.091            | 0.058          | 0.074            | S             | S               |
| NGC3530 | 2.72      | 0.642        | 0.555            | G                | 0.741        | 0.555            | 0.656          | 0.537            | F             | F               |
| NGC3595 | 1.41      | 0.507        | 0.376            | G                | 0.456        | 0.278            | 0.510          | 0.301            | F             | F               |
| NGC3599 | 0.88      | 0.080        | 0.080            | C                | 0.261        | 0.239            | 0.262          | 0.234            | F             | F               |
| NGC3605 | 1.19      | 0.409        | 0.353            | R                | 0.415        | 0.336            | 0.434          | 0.347            | F             | F               |
| NGC3607 | 0.70      | 0.185        | 0.194            | G                | 0.283        | 0.294            | 0.209          | 0.228            | F             | F               |
| NGC3608 | 0.69      | 0.190        | 0.190            | G                | 0.054        | 0.054            | 0.043          | 0.043            | S             | S               |
| NGC3610 | 1.28      | 0.381        | 0.401            | G                | 0.642        | 0.639            | 0.530          | 0.539            | F             | F               |
| NGC3613 | 0.75      | 0.460        | 0.423            | G                | 0.202        | 0.176            | 0.222          | 0.191            | F             | F               |
| NGC3619 | 0.75      | 0.173        | 0.176            | G                | 0.285        | 0.274            | 0.293          | 0.283            | F             | F               |
| NGC3626 | 0.79      | 0.591        | 0.583            | G                | 0.728        | 0.681            | 0.660          | 0.620            | F             | F               |
| NGC3630 | 1.61      | 0.665        | 0.371            | G                | 0.639        | 0.404            | 0.648          | 0.422            | F             | F               |
| NGC3640 | 0.86      | 0.190        | 0.224            | G                | 0.370        | 0.315            | 0.377          | 0.320            | F             | F               |
| NGC3641 | 2.28      | 0.125        | 0.215            | G                | 0.330        | 0.353            | 0.243          | 0.328            | F             | F               |
| NGC3648 | 1.55      | 0.421        | 0.326            | G                | 0.711        | 0.479            | 0.684          | 0.496            | F             | F               |
| NGC3658 | 1.06      | 0.243        | 0.148            | G                | 0.462        | 0.336            | 0.546          | 0.398            | F             | F               |
| NGC3665 | 0.88      | 0.216        | 0.176            | G                | 0.463        | 0.439            | 0.410          | 0.388            | F             | F               |
| NGC3674 | 1.83      | 0.569        | 0.342            | G                | 0.491        | 0.292            | 0.541          | 0.308            | F             | F               |
| NGC3694 | 1.97      | 0.268        | 0.209            | G                | 0.269        | 0.203            | 0.256          | 0.191            | F             | F               |
| NGC3757 | 2.34      | 0.153        | 0.153            | C                | 0.116        | 0.094            | 0.121          | 0.094            | F             | S               |
| NGC3796 | 1.77      | 0.361        | 0.397            | G                | 0.164        | 0.111            | 0.171          | 0.118            | S             | S               |
| NGC3838 | 1.87      | 0.605        | 0.385            | S                | 0.743        | 0.536            | 0.676          | 0.509            | F             | F               |
| NGC3941 | 0.82      | 0.251        | 0.251            | C                | 0.446        | 0.360            | 0.484          | 0.388            | F             | F               |
| NGC3945 | 0.97      | 0.090        | 0.231            | G                | 0.717        | 0.741            | 0.524          | 0.561            | F             | F               |
| NGC3998 | 0.99      | 0.170        | 0.164            | G                | 0.415        | 0.326            | 0.454          | 0.342            | F             | F               |
| NGC4026 | 0.95      | 0.556        | 0.438            | G                | 0.540        | 0.451            | 0.548          | 0.443            | F             | F               |
| NGC4036 | 0.73      | 0.555        | 0.540            | G                | 0.818        | 0.803            | 0.685          | 0.678            | F             | F               |
| NGC4078 | 2.45      | 0.561        | 0.510            | S                | 0.575        | 0.524            | 0.523          | 0.496            | F             | F               |
| NGC4111 | 1.70      | 0.582        | 0.498            | S                | 0.721        | 0.663            | 0.619          | 0.567            | F             | F               |
| NGC4119 | 0.69      | 0.598        | 0.563            | G                | 0.895        | 0.808            | 0.701          | 0.661            | F             | F               |
| NGC4143 | 0.83      | 0.390        | 0.324            | G                | 0.504        | 0.369            | 0.538          | 0.398            | F             | F               |
| NGC4150 | 1.31      | 0.328        | 0.274            | G                | 0.514        | 0.337            | 0.513          | 0.338            | F             | F               |
| NGC4168 | 0.67      | 0.129        | 0.129            | G                | 0.047        | 0.047            | 0.040          | 0.040            | S             | S               |

Table B1 (cont'd)

| Name    | $R_{max}$ | $\epsilon_e$ | $\epsilon_{e/2}$ | $Band(\epsilon)$ | $V/\sigma_e$ | $V/\sigma_{e/2}$ | $\lambda_{R_e}$ | $\lambda_{R_e/2}$ | F/S ( $R_e$ ) | F/S ( $R_e/2$ ) |
|---------|-----------|--------------|------------------|------------------|--------------|------------------|-----------------|-------------------|---------------|-----------------|
| (1)     | (2)       | (3)          | (4)              | (5)              | (6)          | (7)              | (8)             | (9)               | (10)          | (11)            |
| NGC4179 | 1.02      | 0.591        | 0.501            | G                | 0.589        | 0.470            | 0.587           | 0.480             | F             | F               |
| NGC4191 | 1.78      | 0.269        | 0.092            | G                | 0.105        | 0.073            | 0.107           | 0.059             | S             | S               |
| NGC4203 | 0.68      | 0.153        | 0.180            | G                | 0.281        | 0.255            | 0.305           | 0.275             | F             | F               |
| NGC4215 | 1.35      | 0.702        | 0.444            | G                | 0.516        | 0.363            | 0.553           | 0.370             | F             | F               |
| NGC4233 | 1.28      | 0.277        | 0.162            | G                | 0.579        | 0.401            | 0.564           | 0.390             | F             | F               |
| NGC4249 | 1.58      | 0.048        | 0.040            | G                | 0.204        | 0.142            | 0.194           | 0.127             | F             | F               |
| NGC4251 | 1.04      | 0.508        | 0.387            | G                | 0.637        | 0.503            | 0.584           | 0.466             | F             | F               |
| NGC4255 | 1.61      | 0.434        | 0.127            | S                | 0.622        | 0.374            | 0.606           | 0.370             | F             | F               |
| NGC4259 | 2.62      | 0.553        | 0.450            | G                | 0.231        | 0.081            | 0.237           | 0.068             | F             | S               |
| NGC4261 | 0.53      | 0.222        | 0.222            | G                | 0.090        | 0.090            | 0.085           | 0.085             | S             | S               |
| NGC4262 | 1.65      | 0.117        | 0.117            | C                | 0.295        | 0.251            | 0.308           | 0.245             | F             | F               |
| NGC4264 | 1.49      | 0.191        | 0.191            | C                | 0.534        | 0.336            | 0.490           | 0.316             | F             | F               |
| NGC4267 | 0.70      | 0.079        | 0.079            | C                | 0.238        | 0.230            | 0.246           | 0.233             | F             | F               |
| NGC4268 | 1.22      | 0.552        | 0.348            | G                | 0.491        | 0.333            | 0.492           | 0.330             | F             | F               |
| NGC4270 | 1.23      | 0.543        | 0.424            | G                | 0.378        | 0.289            | 0.406           | 0.295             | F             | F               |
| NGC4278 | 0.82      | 0.103        | 0.134            | G                | 0.201        | 0.208            | 0.178           | 0.203             | F             | F               |
| NGC4281 | 0.92      | 0.535        | 0.502            | G                | 0.757        | 0.703            | 0.651           | 0.621             | F             | F               |
| NGC4283 | 1.68      | 0.033        | 0.031            | G                | 0.172        | 0.155            | 0.171           | 0.151             | F             | F               |
| NGC4324 | 1.02      | 0.434        | 0.197            | G                | 0.639        | 0.407            | 0.592           | 0.389             | F             | F               |
| NGC4339 | 0.68      | 0.060        | 0.060            | G                | 0.311        | 0.302            | 0.325           | 0.312             | F             | F               |
| NGC4340 | 0.72      | 0.227        | 0.237            | G                | 0.499        | 0.481            | 0.458           | 0.442             | F             | F               |
| NGC4342 | 3.08      | 0.442        | 0.263            | S                | 0.537        | 0.307            | 0.528           | 0.306             | F             | F               |
| NGC4346 | 1.05      | 0.533        | 0.360            | G                | 0.571        | 0.428            | 0.576           | 0.439             | F             | F               |
| NGC4350 | 1.16      | 0.674        | 0.550            | G                | 0.658        | 0.460            | 0.638           | 0.480             | F             | F               |
| NGC4365 | 0.48      | 0.254        | 0.254            | G                | 0.114        | 0.114            | 0.088           | 0.088             | S             | S               |
| NGC4371 | 0.70      | 0.309        | 0.313            | G                | 0.541        | 0.541            | 0.482           | 0.482             | F             | F               |
| NGC4374 | 0.58      | 0.147        | 0.147            | G                | 0.026        | 0.026            | 0.024           | 0.024             | S             | S               |
| NGC4377 | 1.47      | 0.157        | 0.228            | S                | 0.443        | 0.314            | 0.473           | 0.338             | F             | F               |
| NGC4379 | 1.08      | 0.224        | 0.258            | G                | 0.386        | 0.294            | 0.398           | 0.300             | F             | F               |
| NGC4382 | 0.39      | 0.202        | 0.202            | G                | 0.174        | 0.174            | 0.163           | 0.163             | F             | F               |
| NGC4387 | 1.24      | 0.373        | 0.351            | G                | 0.391        | 0.315            | 0.399           | 0.317             | F             | F               |
| NGC4406 | 0.28      | 0.211        | 0.211            | G                | 0.090        | 0.090            | 0.052           | 0.052             | S             | S               |
| NGC4417 | 1.15      | 0.566        | 0.418            | G                | 0.542        | 0.395            | 0.547           | 0.392             | F             | F               |
| NGC4425 | 0.85      | 0.676        | 0.587            | G                | 0.438        | 0.363            | 0.454           | 0.384             | F             | F               |
| NGC4429 | 0.66      | 0.402        | 0.402            | G                | 0.455        | 0.455            | 0.397           | 0.397             | F             | F               |
| NGC4434 | 1.41      | 0.058        | 0.082            | G                | 0.249        | 0.186            | 0.288           | 0.199             | F             | F               |
| NGC4435 | 0.64      | 0.468        | 0.465            | G                | 0.672        | 0.667            | 0.599           | 0.597             | F             | F               |
| NGC4442 | 0.73      | 0.335        | 0.307            | G                | 0.350        | 0.329            | 0.363           | 0.338             | F             | F               |
| NGC4452 | 0.97      | 0.880        | 0.880            | G                | 0.765        | 0.765            | 0.648           | 0.648             | F             | F               |
| NGC4458 | 0.85      | 0.121        | 0.118            | G                | 0.150        | 0.161            | 0.072           | 0.079             | S             | S               |
| NGC4459 | 0.74      | 0.148        | 0.128            | G                | 0.477        | 0.450            | 0.438           | 0.408             | F             | F               |
| NGC4461 | 0.82      | 0.392        | 0.306            | G                | 0.486        | 0.405            | 0.511           | 0.430             | F             | F               |
| NGC4472 | 0.30      | 0.172        | 0.172            | G                | 0.073        | 0.073            | 0.077           | 0.077             | S             | S               |
| NGC4473 | 0.92      | 0.421        | 0.396            | G                | 0.255        | 0.263            | 0.230           | 0.250             | F             | F               |
| NGC4474 | 0.99      | 0.570        | 0.468            | G                | 0.439        | 0.347            | 0.446           | 0.353             | F             | F               |
| NGC4476 | 1.28      | 0.353        | 0.375            | G                | 0.236        | 0.298            | 0.153           | 0.266             | S             | F               |
| NGC4477 | 0.52      | 0.135        | 0.135            | C                | 0.211        | 0.211            | 0.213           | 0.213             | F             | F               |
| NGC4478 | 1.26      | 0.165        | 0.175            | G                | 0.221        | 0.175            | 0.233           | 0.177             | F             | F               |
| NGC4483 | 1.16      | 0.346        | 0.251            | G                | 0.474        | 0.271            | 0.465           | 0.273             | F             | F               |
| NGC4486 | 0.38      | 0.037        | 0.037            | G                | 0.024        | 0.024            | 0.021           | 0.021             | S             | S               |

Table B1 (cont'd)

| Name     | $R_{max}$ | $\epsilon_e$ | $\epsilon_{e/2}$ | $Band(\epsilon)$ | $V/\sigma_e$ | $V/\sigma_{e/2}$ | $\lambda_{Re}$ | $\lambda_{Re/2}$ | F/S ( $R_e$ ) | F/S ( $R_e/2$ ) |
|----------|-----------|--------------|------------------|------------------|--------------|------------------|----------------|------------------|---------------|-----------------|
| (1)      | (2)       | (3)          | (4)              | (5)              | (6)          | (7)              | (8)            | (9)              | (10)          | (11)            |
| NGC4486A | 2.23      | 0.224        | 0.224            | G                | 0.379        | 0.379            | 0.351          | 0.351            | F             | F               |
| NGC4489  | 0.77      | 0.085        | 0.075            | G                | 0.176        | 0.125            | 0.168          | 0.117            | F             | F               |
| NGC4494  | 0.56      | 0.173        | 0.173            | G                | 0.219        | 0.219            | 0.212          | 0.212            | F             | F               |
| NGC4503  | 0.74      | 0.446        | 0.429            | G                | 0.510        | 0.451            | 0.523          | 0.470            | F             | F               |
| NGC4521  | 1.22      | 0.566        | 0.483            | G                | 0.794        | 0.566            | 0.682          | 0.534            | F             | F               |
| NGC4526  | 0.59      | 0.361        | 0.361            | G                | 0.563        | 0.563            | 0.453          | 0.453            | F             | F               |
| NGC4528  | 1.42      | 0.392        | 0.129            | G                | 0.112        | 0.116            | 0.096          | 0.102            | S             | F               |
| NGC4546  | 0.82      | 0.527        | 0.465            | G                | 0.653        | 0.572            | 0.639          | 0.579            | F             | F               |
| NGC4550  | 1.32      | 0.649        | 0.634            | G                | 0.122        | 0.072            | 0.105          | 0.061            | S             | S               |
| NGC4551  | 1.21      | 0.284        | 0.259            | G                | 0.311        | 0.285            | 0.295          | 0.259            | F             | F               |
| NGC4552  | 0.59      | 0.047        | 0.047            | G                | 0.051        | 0.051            | 0.049          | 0.049            | S             | S               |
| NGC4564  | 1.06      | 0.560        | 0.477            | G                | 0.640        | 0.532            | 0.619          | 0.536            | F             | F               |
| NGC4570  | 0.97      | 0.626        | 0.551            | G                | 0.587        | 0.470            | 0.603          | 0.498            | F             | F               |
| NGC4578  | 0.84      | 0.289        | 0.282            | G                | 0.669        | 0.596            | 0.596          | 0.544            | F             | F               |
| NGC4596  | 0.67      | 0.254        | 0.254            | C                | 0.301        | 0.289            | 0.284          | 0.264            | F             | F               |
| NGC4608  | 0.77      | 0.229        | 0.229            | C                | 0.179        | 0.171            | 0.178          | 0.168            | F             | F               |
| NGC4612  | 0.96      | 0.204        | 0.196            | R                | 0.428        | 0.345            | 0.407          | 0.324            | F             | F               |
| NGC4621  | 0.60      | 0.365        | 0.364            | G                | 0.273        | 0.272            | 0.291          | 0.291            | F             | F               |
| NGC4623  | 1.01      | 0.673        | 0.648            | G                | 0.660        | 0.602            | 0.598          | 0.564            | F             | F               |
| NGC4624  | 0.62      | 0.065        | 0.065            | C                | 0.240        | 0.240            | 0.236          | 0.236            | F             | F               |
| NGC4636  | 0.29      | 0.094        | 0.094            | G                | 0.039        | 0.039            | 0.036          | 0.036            | S             | S               |
| NGC4638  | 1.24      | 0.606        | 0.657            | G                | 0.909        | 0.895            | 0.691          | 0.714            | F             | F               |
| NGC4643  | 0.83      | 0.249        | 0.199            | G                | 0.321        | 0.323            | 0.255          | 0.254            | F             | F               |
| NGC4649  | 0.41      | 0.156        | 0.156            | G                | 0.123        | 0.123            | 0.127          | 0.127            | F             | F               |
| NGC4660  | 1.64      | 0.441        | 0.315            | G                | 0.603        | 0.518            | 0.553          | 0.476            | F             | F               |
| NGC4684  | 0.97      | 0.597        | 0.596            | G                | 0.713        | 0.665            | 0.622          | 0.600            | F             | F               |
| NGC4690  | 1.14      | 0.266        | 0.257            | G                | 0.149        | 0.130            | 0.151          | 0.123            | S             | S               |
| NGC4694  | 0.69      | 0.547        | 0.546            | G                | 0.275        | 0.276            | 0.289          | 0.295            | F             | F               |
| NGC4697  | 0.44      | 0.447        | 0.447            | G                | 0.363        | 0.363            | 0.322          | 0.322            | F             | F               |
| NGC4710  | 0.73      | 0.699        | 0.395            | G                | 0.731        | 0.496            | 0.652          | 0.456            | F             | F               |
| NGC4733  | 0.83      | 0.060        | 0.060            | C                | 0.095        | 0.088            | 0.085          | 0.076            | F             | F               |
| NGC4753  | 0.56      | 0.213        | 0.213            | G                | 0.537        | 0.537            | 0.467          | 0.467            | F             | F               |
| NGC4754  | 0.82      | 0.480        | 0.480            | C                | 0.423        | 0.366            | 0.433          | 0.369            | F             | F               |
| NGC4762  | 0.44      | 0.852        | 0.852            | G                | 0.783        | 0.783            | 0.724          | 0.724            | F             | F               |
| NGC4803  | 2.38      | 0.282        | 0.266            | S                | 0.192        | 0.063            | 0.181          | 0.054            | F             | S               |
| NGC5103  | 1.90      | 0.594        | 0.400            | G                | 0.588        | 0.370            | 0.573          | 0.386            | F             | F               |
| NGC5173  | 1.96      | 0.133        | 0.124            | G                | 0.165        | 0.110            | 0.168          | 0.106            | F             | F               |
| NGC5198  | 0.84      | 0.146        | 0.151            | G                | 0.074        | 0.072            | 0.061          | 0.057            | S             | S               |
| NGC5273  | 0.72      | 0.108        | 0.116            | G                | 0.554        | 0.512            | 0.517          | 0.482            | F             | F               |
| NGC5308  | 1.02      | 0.735        | 0.637            | G                | 0.641        | 0.478            | 0.651          | 0.510            | F             | F               |
| NGC5322  | 0.65      | 0.307        | 0.304            | G                | 0.126        | 0.121            | 0.073          | 0.067            | S             | S               |
| NGC5342  | 1.93      | 0.586        | 0.425            | G                | 0.638        | 0.410            | 0.626          | 0.439            | F             | F               |
| NGC5353  | 1.00      | 0.552        | 0.541            | G                | 0.689        | 0.544            | 0.618          | 0.532            | F             | F               |
| NGC5355  | 1.74      | 0.296        | 0.263            | G                | 0.288        | 0.214            | 0.286          | 0.211            | F             | F               |
| NGC5358  | 1.87      | 0.592        | 0.395            | G                | 0.675        | 0.461            | 0.610          | 0.442            | F             | F               |
| NGC5379  | 0.96      | 0.627        | 0.696            | G                | 0.920        | 0.794            | 0.719          | 0.677            | F             | F               |
| NGC5422  | 0.85      | 0.604        | 0.537            | G                | 0.588        | 0.476            | 0.600          | 0.501            | F             | F               |
| NGC5473  | 0.94      | 0.211        | 0.211            | C                | 0.372        | 0.306            | 0.371          | 0.291            | F             | F               |
| NGC5475  | 1.25      | 0.696        | 0.568            | G                | 0.965        | 0.711            | 0.759          | 0.638            | F             | F               |
| NGC5481  | 0.89      | 0.214        | 0.161            | G                | 0.159        | 0.165            | 0.103          | 0.091            | S             | S               |

Table B1 (cont'd)

| Name      | $R_{max}$ | $\epsilon_e$ | $\epsilon_{e/2}$ | $Band(\epsilon)$ | $V/\sigma_e$ | $V/\sigma_{e/2}$ | $\lambda_{R_e}$ | $\lambda_{R_{e/2}}$ | F/S ( $R_e$ ) | F/S ( $R_e/2$ ) |
|-----------|-----------|--------------|------------------|------------------|--------------|------------------|-----------------|---------------------|---------------|-----------------|
| (1)       | (2)       | (3)          | (4)              | (5)              | (6)          | (7)              | (8)             | (9)                 | (10)          | (11)            |
| NGC5485   | 0.70      | 0.171        | 0.208            | G                | 0.176        | 0.160            | 0.165           | 0.149               | F             | F               |
| NGC5493   | 1.44      | 0.561        | 0.640            | G                | 1.095        | 1.089            | 0.740           | 0.773               | F             | F               |
| NGC5500   | 1.34      | 0.234        | 0.214            | G                | 0.178        | 0.155            | 0.172           | 0.146               | F             | F               |
| NGC5507   | 1.61      | 0.252        | 0.144            | G                | 0.479        | 0.302            | 0.495           | 0.306               | F             | F               |
| NGC5557   | 0.69      | 0.169        | 0.157            | G                | 0.048        | 0.044            | 0.049           | 0.045               | S             | S               |
| NGC5574   | 1.48      | 0.627        | 0.566            | G                | 0.443        | 0.371            | 0.452           | 0.381               | F             | F               |
| NGC5576   | 0.90      | 0.307        | 0.310            | G                | 0.097        | 0.088            | 0.102           | 0.091               | S             | S               |
| NGC5582   | 0.73      | 0.320        | 0.321            | G                | 0.676        | 0.668            | 0.564           | 0.567               | F             | F               |
| NGC5611   | 2.04      | 0.559        | 0.485            | G                | 0.816        | 0.661            | 0.691           | 0.590               | F             | F               |
| NGC5631   | 0.96      | 0.127        | 0.167            | G                | 0.171        | 0.193            | 0.110           | 0.166               | S             | F               |
| NGC5638   | 0.71      | 0.091        | 0.079            | G                | 0.253        | 0.222            | 0.265           | 0.229               | F             | F               |
| NGC5687   | 0.86      | 0.379        | 0.349            | G                | 0.486        | 0.440            | 0.479           | 0.435               | F             | F               |
| NGC5770   | 1.16      | 0.061        | 0.061            | C                | 0.248        | 0.168            | 0.290           | 0.168               | F             | F               |
| NGC5813   | 0.48      | 0.170        | 0.170            | G                | 0.161        | 0.161            | 0.071           | 0.071               | S             | S               |
| NGC5831   | 0.94      | 0.136        | 0.203            | G                | 0.088        | 0.092            | 0.063           | 0.065               | S             | S               |
| NGC5838   | 0.80      | 0.361        | 0.297            | G                | 0.521        | 0.464            | 0.521           | 0.460               | F             | F               |
| NGC5839   | 1.19      | 0.100        | 0.169            | G                | 0.385        | 0.269            | 0.430           | 0.298               | F             | F               |
| NGC5845   | 3.23      | 0.264        | 0.236            | G                | 0.402        | 0.368            | 0.404           | 0.358               | F             | F               |
| NGC5846   | 0.47      | 0.062        | 0.062            | R                | 0.037        | 0.037            | 0.032           | 0.032               | S             | S               |
| NGC5854   | 1.09      | 0.575        | 0.426            | G                | 0.761        | 0.531            | 0.678           | 0.515               | F             | F               |
| NGC5864   | 0.89      | 0.695        | 0.658            | G                | 0.630        | 0.556            | 0.603           | 0.550               | F             | F               |
| NGC5866   | 0.56      | 0.565        | 0.565            | G                | 0.349        | 0.349            | 0.319           | 0.319               | F             | F               |
| NGC5869   | 0.98      | 0.245        | 0.244            | G                | 0.433        | 0.387            | 0.428           | 0.383               | F             | F               |
| NGC6010   | 1.32      | 0.742        | 0.539            | G                | 0.703        | 0.555            | 0.679           | 0.556               | F             | F               |
| NGC6014   | 0.90      | 0.419        | 0.434            | G                | 0.418        | 0.378            | 0.387           | 0.353               | F             | F               |
| NGC6017   | 2.83      | 0.455        | 0.405            | G                | 0.441        | 0.352            | 0.429           | 0.340               | F             | F               |
| NGC6149   | 1.89      | 0.325        | 0.279            | G                | 0.656        | 0.579            | 0.563           | 0.513               | F             | F               |
| NGC6278   | 1.23      | 0.409        | 0.401            | G                | 0.521        | 0.368            | 0.576           | 0.411               | F             | F               |
| NGC6547   | 1.73      | 0.674        | 0.456            | G                | 0.616        | 0.411            | 0.633           | 0.444               | F             | F               |
| NGC6548   | 1.02      | 0.107        | 0.107            | C                | 0.258        | 0.236            | 0.253           | 0.227               | F             | F               |
| NGC6703   | 0.88      | 0.019        | 0.017            | G                | 0.043        | 0.038            | 0.041           | 0.035               | S             | F               |
| NGC6798   | 1.20      | 0.461        | 0.372            | G                | 0.488        | 0.322            | 0.483           | 0.310               | F             | F               |
| NGC7280   | 0.95      | 0.363        | 0.377            | G                | 0.606        | 0.538            | 0.557           | 0.503               | F             | F               |
| NGC7332   | 1.12      | 0.674        | 0.469            | G                | 0.490        | 0.291            | 0.561           | 0.338               | F             | F               |
| NGC7454   | 0.79      | 0.364        | 0.363            | R                | 0.106        | 0.091            | 0.094           | 0.067               | S             | S               |
| NGC7457   | 0.69      | 0.470        | 0.438            | G                | 0.546        | 0.478            | 0.519           | 0.465               | F             | F               |
| NGC7465   | 2.51      | 0.364        | 0.406            | G                | 0.343        | 0.352            | 0.283           | 0.294               | F             | F               |
| NGC7693   | 1.55      | 0.233        | 0.275            | G                | 0.686        | 0.440            | 0.616           | 0.408               | F             | F               |
| NGC7710   | 2.42      | 0.580        | 0.548            | S                | 0.293        | 0.136            | 0.340           | 0.137               | F             | S               |
| PGC016060 | 1.93      | 0.694        | 0.681            | G                | 1.019        | 0.682            | 0.759           | 0.616               | F             | F               |
| PGC028887 | 1.83      | 0.323        | 0.312            | G                | 0.282        | 0.332            | 0.145           | 0.252               | S             | F               |
| PGC029321 | 2.69      | 0.140        | 0.146            | G                | 0.339        | 0.187            | 0.336           | 0.175               | F             | F               |
| PGC035754 | 3.00      | 0.275        | 0.333            | G                | 0.258        | 0.275            | 0.210           | 0.266               | F             | F               |
| PGC042549 | 1.78      | 0.369        | 0.450            | G                | 0.771        | 0.560            | 0.673           | 0.529               | F             | F               |
| PGC044433 | 3.92      | 0.335        | 0.184            | S                | 0.362        | 0.205            | 0.357           | 0.200               | F             | F               |
| PGC050395 | 1.84      | 0.233        | 0.240            | G                | 0.149        | 0.111            | 0.138           | 0.089               | S             | S               |
| PGC051753 | 2.03      | 0.549        | 0.538            | G                | 0.668        | 0.538            | 0.587           | 0.513               | F             | F               |
| PGC054452 | 1.42      | 0.189        | 0.175            | G                | 0.434        | 0.316            | 0.416           | 0.307               | F             | F               |
| PGC056772 | 2.37      | 0.493        | 0.467            | G                | 0.386        | 0.443            | 0.310           | 0.420               | F             | F               |
| PGC058114 | 2.19      | 0.185        | 0.213            | R                | 0.228        | 0.159            | 0.176           | 0.132               | F             | F               |

Table B1 (cont'd)

| Name      | $R_{max}$ | $\epsilon_e$ | $\epsilon_{e/2}$ | Band( $\epsilon$ ) | $V/\sigma_e$ | $V/\sigma_{e/2}$ | $\lambda_{R_e}$ | $\lambda_{R_e/2}$ | F/S ( $R_e$ ) | F/S ( $R_e/2$ ) |
|-----------|-----------|--------------|------------------|--------------------|--------------|------------------|-----------------|-------------------|---------------|-----------------|
| (1)       | (2)       | (3)          | (4)              | (5)                | (6)          | (7)              | (8)             | (9)               | (10)          | (11)            |
| PGC061468 | 1.75      | 0.231        | 0.230            | G                  | 0.464        | 0.391            | 0.409           | 0.360             | F             | F               |
| PGC071531 | 2.69      | 0.305        | 0.235            | R                  | 0.323        | 0.263            | 0.333           | 0.266             | F             | F               |
| PGC170172 | 2.44      | 0.195        | 0.372            | G                  | 0.287        | 0.192            | 0.324           | 0.218             | F             | F               |
| UGC03960  | 1.16      | 0.190        | 0.081            | G                  | 0.130        | 0.109            | 0.119           | 0.094             | S             | F               |
| UGC04551  | 1.91      | 0.137        | 0.137            | G                  | 0.252        | 0.205            | 0.277           | 0.214             | F             | F               |
| UGC05408  | 3.08      | 0.168        | 0.248            | G                  | 0.290        | 0.270            | 0.278           | 0.292             | F             | F               |
| UGC06062  | 1.75      | 0.449        | 0.449            | C                  | 0.447        | 0.300            | 0.449           | 0.295             | F             | F               |
| UGC06176  | 1.88      | 0.253        | 0.330            | G                  | 0.670        | 0.447            | 0.585           | 0.426             | F             | F               |
| UGC08876  | 2.40      | 0.408        | 0.180            | S                  | 0.311        | 0.182            | 0.341           | 0.189             | F             | F               |
| UGC09519  | 2.77      | 0.483        | 0.407            | G                  | 0.764        | 0.631            | 0.632           | 0.552             | F             | F               |

Note. — Columns (1): Galaxy Name from the principal designation from LEDA; (2): largest equivalent aperture radius reached by the SAURON maps in units of  $R_e$ ; (3) and (4): moment ellipticity measured within one effective radius  $R_e$  and one half effective radius  $R_e/2$ , these being replaced by the global ellipticity measured from the outer isophotes for galaxies with clear bars (see text) as indicated by a "C" in column (5) of this table; (5) "Band" refers to the source of the radial ellipticity profiles, with G, R and S referring to the Green, Red and Sauron photometry, and "C" for galaxies which have strong bars significantly affecting the measurement of  $\epsilon_e$ , and for which the outer ellipticity measurement  $\epsilon_{glob}$  (see Paper II) is used instead; (6) and (7)  $V/\sigma$  as measured within  $1 R_e$  and  $R_e/2$ ; (8) and (9):  $\lambda_R$  measured within  $1 R_e$  and  $R_e/2$ ; (10) and (11) Fast (F) or Slow (S) Rotator according to the  $\lambda_R$  and  $\epsilon$  values at  $R_e$  and  $R_e/2$ .